Evaluating Energy and Visibility Trade-offs in LEO Satellite Edge Computing for Airplane Detection

Eomji Kim

A thesis
submitted in partial fulfillment of the
requirements for the degree of

Master of Science

University of Washington

2025

Committee:

Mehran Mesbahi

Amir Taghvaei

Program Authorized to Offer Degree:
Aeronautics and Astronautic

University of Washington

Abstract

Evaluating Energy and Visibility Trade-offs in
LEO Satellite Edge Computing for Airplane Detection

Eomji Kim

Chair of the Supervisory Committee:
Mehran Mesbahi

This thesis investigates the efficiency of various LEO configurations for autonomous airplane detection using onboard edge computing in space. The study evaluates the trade-off between maximizing target visibility—defined as daytime passes suitable for optical detection over Incheon International Airport—and minimizing energy consumption for satellite operations.

A baseline Sun-Synchronous Orbit (SSO) is compared against multiple Non-Sun-Synchronous Orbits (NSSOs) with varying inclinations (45°–110°), RAANs, and arguments of perigee. For each configuration, orbital visibility is simulated over 1-day and 7-day windows using Python-based tools with J2 perturbation modeling validated against GMAT. Daytime visibility is filtered using local KST-based illumination constraints.

To quantify operational efficiency, a composite scoring system is introduced that aggregates normalized visibility metrics, followed by an energy modeling framework estimating consumption per image strip and per orbit. The model incorporates realistic assumptions: an optical payload based on KOMPSAT-3 specifications, onboard inference with YOLOv5n on NVIDIA Jetson Xavier NX, and S-band downlink of detection results. A simplified solar generation model evaluates the power budget.

The findings reveal that mid-inclination NSSOs (especially at 70°) strike the most effective balance between data yield and energy sustainability. The methodology provides a scalable framework for orbit design tailored to edge-AI missions requiring both high revisit rates and energy efficiency.

TABLE OF CONTENTS

LIST OF FIGURES

LIST OF TABLES

GLOSSARY

ADCS (Attitude Determination and Control System): The satellite subsystem responsible for determining and controlling the satellite's orientation (pointing). Assumed to have pointed the sensor correctly prior to image capture in this study.

AOP (Argument of Perigee): An orbital element representing the angle from the ascending node to the orbit's closest point to Earth (perigee), measured within the orbital plane.

CUDA (Compute Unified Device Architecture): NVIDIA's special technology that lets software (like PyTorch and TensorRT) use the powerful calculation abilities of NVIDIA graphics cards (GPUs) to speed up demanding tasks like AI.

Daytime Pass: A satellite pass over Incheon International Airport (ICN) (above 20° elevation) occurring when the sun is above the local horizon, determined using Korea Standard Time (KST) sunrise/sunset data. Only these passes trigger active payload energy consumption in the model.

ECI (Earth-Centered Inertial): A non-rotating reference frame centered at Earth's center, used for precise orbit modeling.

Edge Computing: Performing data processing (YOLOv5n inference) directly on the satellite platform to reduce data downlink volume and latency. The energy cost of this onboard processing is analyzed.

Epoch: The fixed starting time for all orbit simulations (March 20, 2025, 00:00 UTC), ensuring consistent initial conditions.

FPS (Frames Per Second): A measure of speed indicating how many images (or image tiles) the AI model can process per second during inference. Higher FPS means faster processing.

GMAT (General Mission Analysis Tool): NASA's orbit analysis software used here solely to validate baseline trajectories from the primary Python propagator.

GSD (Ground Sample Distance): A measure of image spatial resolution, representing the ground area covered by a single pixel. GSD increases for off-nadir angles due to longer slant range.

GPU (Graphics Processing Unit): Specialized processor optimized for parallel computations, used via CUDA to accelerate AI inference on the assumed Jetson Xavier NX hardware.

Inclination: An orbital element defining the angle between the orbital plane and the Earth's equator. Varied from 45° to 110° in this study to compare different orbit types.

Inference: The process of using the trained YOLOv5n model on the edge hardware to detect airplanes in a captured image tile. Its time (`t_process`) and power (`P_process`) are key energy model inputs.

Jetson Xavier NX: An NVIDIA embedded computing board with an integrated GPU, assumed as the onboard edge processing hardware for running YOLOv5n in this study's energy model.

J2 Perturbation: A gravitational perturbation caused by Earth's equatorial bulge, primarily responsible for long-term RAAN and AOP drift in LEO orbits.

KST (Korea Standard Time): The time zone for South Korea (UTC+9). Used in this study to determine local daytime at the target location (Incheon International Airport).

LEO (Low Earth Orbit): Orbits below 2000 km altitude, such as the 685 km orbit used in this study. Offers potential for higher resolution and revisit frequency.

LVLH (Local Vertical Local Horizontal): A local reference frame fixed to the satellite's orbit used for orientation and solar exposure modeling. The +Z axis points toward Earth's center (nadir), the +Y axis is aligned opposite to the orbital angular momentum vector (normal to the orbital plane), and the +X axis completes the right-handed system (in the direction of satellite velocity).

MLST (Mean Local Solar Time): The average local solar time when a satellite passes over a given location. SSO maintains constant MLST; NSSO does not.

Mean Anomaly (M0): An orbital element describing the satellite's position along its orbit at a given epoch.

mAP (mean Average Precision): A standard metric for evaluating object detection model accuracy. Used here to confirm YOLOv5n's baseline effectiveness.

NSSO (Non-Sun-Synchronous Orbit): A LEO where the satellite passes over locations at varying local solar times due to its orbital plane's precession rate not matching the Sun's apparent movement. This study analyzes various NSSO configurations against the SSO baseline, considering potential trade-offs in revisit frequency and illumination consistency.

Off-nadir: A viewing geometry where the sensor is angled away from directly downward (nadir), reducing resolution and increasing slant range.

Pass: A continuous period when the satellite is visible above the 20° minimum elevation angle from Incheon International Airport (ICN). Visibility metrics quantify pass characteristics (duration, count).

Payload: The mission-specific equipment, here comprising the optical imager and the edge computing hardware. Its energy consumption during active cycles is modeled.

PyTorch: An open-source machine learning library used to train the YOLOv5n model. The energy model focuses on the inference stage after training.

RAAN (Right Ascension of the Ascending Node): An orbital element that specifies the angle from a fixed direction (typically the vernal equinox) to the ascending node of the orbit.

Slant Range: The direct line-of-sight distance between the satellite and the ground target; increases for off-nadir imaging.

SSO (Sun-Synchronous Orbit): A LEO orbit passing over locations at the same local solar time daily, providing consistent lighting. Serves as the baseline for comparison.

TensorRT: An NVIDIA library for optimizing trained deep learning models (like YOLOv5n) for faster inference on NVIDIA GPUs. Its use is assumed for performance estimates.

Tile: A cropped sub-region of an image strip processed individually by the onboard AI. Multiple tiles are generated from one strip.

Tiling: Dividing the large captured image strip into smaller, overlapping patches (tiles) suitable for input to the fixed-size YOLOv5n model. The energy model accounts for processing multiple tiles per capture.

TOPS (Tera Operations Per Second): A performance measure of AI hardware representing how many trillion operations it can perform per second.

UTC (Coordinated Universal Time): The primary time standard used globally and as the basis for simulation time and satellite ephemeris data.

YOLOv5n (You Only Look Once version 5 nano): The specific lightweight object detection AI model used for simulated onboard processing. Chosen for its efficiency and acceptable accuracy.

ACKNOWLEDGMENTS

I would first like to express my deepest gratitude to Professor Mehran Mesbahi, my advisor, for guiding me through this entirely new world of aerospace. Coming from a non-engineering background, I struggled even to choose a direction, but his support and insight gave me clarity when I needed it most, and made graduation possible.

I also sincerely thank Professor Amir Taghvaei, whose excellent teaching in core control courses gave me the foundation I needed to progress in this field. I am grateful for his willingness to serve on my committee and for his thoughtful feedback on this project.

To the members of RAIN Lab, thank you for your patience, encouragement, and generosity — not only in helping me through difficult technical questions but also in welcoming me as a part of the team. Your support, feedback, and friendship meant more than I can express.

To my UW friends, thank you for reminding me that exploring a new country and creating meaningful memories is also part of this journey. Your positive energy and steady encouragement lifted me in more ways than you know.

I also extend to thank the ROK Army for being a long-time source of professional experience and for supporting my pursuit of this academic challenge.

I would like to thank Professor Sojin Park, Lieutenant Colonel Jongdeok Yoon, and Lieutenant Colonel Hunsik Lee for their kind encouragement and support during my graduate application process.

Finally, to my family, friends, and colleagues in Korea — thank you for cheering me on from afar, celebrating my challenges as your own victories. Your unwavering support gave me the strength to keep going, every step of the way.

.

DEDICATION

To peace and better life

Chapter 1

INTRODUCTION

Beyond ground-based surveillance like CCTV and radar, numerous space-based assets monitor terrestrial situations. Increasingly, the sensors aboard numerous satellites, especially smaller ones, operate with greater autonomy, managed by sophisticated onboard computing systems. This capability is crucial as satellite surveillance (used for commercial, private, and military purposes) is becoming ever more vital as the pace of global change accelerates. In today's dynamic world, the timeliness of information is often as critical as its accuracy; delays in situational awareness and decision-making can lead to significant negative consequences. Consider, for example, an unidentified airplane: its rapid movement could quickly pose a threat to civilian air traffic or military operations [3]. The potential for such fast-evolving threats is a key reason why responsive, intelligent space-based monitoring technologies are advancing so rapidly.

A key advancement enabling smarter surveillance satellites involves integrating edge computing hardware directly onboard the spacecraft. Traditionally, satellites collect raw data and transmit the entire, unprocessed dataset to ground stations. This large volume of raw data, however, often strains downlink capacity, leading to significant transmission delays and high energy consumption, that consequently can shorten a satellite's operational lifespan. In order to mitigate these challenges of latency and energy expenditure, computing capabilities are now commonly integrated directly onboard the satellite platform. This allows an onboard computer to analyze and process data locally, transmitting only essential or prioritized information to the ground. This onboard processing significantly improves mission efficiency and reduces data turnaround time, mainly because analysis occurs immediately upon capture and the volume of transmitted data is drastically reduced [4]. At the same time, edge computing hardware has improved, allowing more complex computations be performed directly onboard [5, 6]. This improved hardware, furthermore, facilitates the use of continually developing AI algorithms optimized for specific tasks. Examples include variants of the You Only Look Once (YOLO) architecture [7]. Models leveraging frameworks such as TensorFlow

Lite [8] or tools like TensorRT [5] for optimization are also finding wide range of applications within these satellite edge computing systems [6]. The integration of advanced edge hardware and intelligent algorithms onto satellites marks the dawn of the new era of responsive space assets.

1.1 *Orbital Considerations and Trade-offs for Edge AI Missions*

While onboard edge computing and AI significantly enhance satellite capabilities, the ultimate success of autonomous surveillance missions is still critically dependent on the chosen orbit. The satellite's orbit determines key operational factors, such as the frequency and duration of viewing opportunities over a specific target region, like Incheon Airport (ICN). Additionally, for missions using optical sensors, the orbit sets the lighting conditions during target encounters. Proper illumination is essential for acquiring high-quality imagery and ensuring reliable performance from onboard AI analysis algorithms [9]. These key characteristics – primarily revisit timing and lighting conditions – are defined by the satellite's main orbital elements. These elements include altitude, inclination, Right Ascension of the Ascending Node (RAAN), Argument of Perigee (AOP), and the satellite's position along its path (often related to Mean Anomaly) [1]. Therefore, careful simulation and analysis during the mission design phase are necessary to select an orbit that optimizes both mission success and overall efficiency.

The satellite's power budget throughout the mission duration is another critical factor to consider in mission design. Onboard power typically comes from solar panels and is stored in batteries for continuous operation. Because this power source is inherently limited, careful planning of energy use is essential to ensure the satellite can function for its intended lifetime. Furthermore, there is a common trend to reduce satellite size and mass to lower launch costs [10]; however, this usually means less surface area is available for power-generating components like solar panels. Therefore, missions that require significant amounts of energy, such as surveillance tasks involving active sensors and considerable onboard data processing, face major power constraints.

These surveillance missions are typically energy-intensive, primarily as they require the acquisition of specific data products, such as high-resolution imagery and precise coordinates, often combined with rapid onboard processing or data transmission cycles needed for timely decision support. Operational tasks including target geolocation, image acquisition, and particularly the

computationally demanding onboard data analysis using complex AI algorithms, contribute significantly to this energy usage [11]. Generally, increased computational complexity for these onboard operations directly corresponds to higher power consumption. As a result, the constrained onboard power supply creates a fundamental dilemma for mission planning: the objective of maximizing valuable observation time, essential for mission performance, directly conflicts with the critical need to manage finite energy resources to ensure the satellite can operate throughout its planned mission lifetime.

To effectively navigate the trade-off between securing sufficient observation time and operating within finite energy constraints, two primary types of LEO will be compared in this study. The first is SSO and the second is NSSO. One representative SSO and two representative NSSOs (selected because the potential parameter range for NSSO is much larger) will be analyzed.

SSO maintains a nearly constant solar orientation, ensuring consistent Mean Local Solar Time (MLST) for passes. This provides stable illumination beneficial for optical sensors [1, 12, 13] and simplifies onboard AI analysis [11]. However, it limits observation times and revisits the flexibility for specific targets.

NSSOs lack fixed solar orientation, resulting in varying local solar times for passes. This offers operational flexibility for the frequency of re-visitation and the diverse observation times, overcoming the SSO limitations [1]. However, this orbital geometry complicates the prediction of the return times and illumination, potentially degrading optical image quality and requiring more robust AI algorithms onboard [9].

Given the distinct characteristics of SSO and NSSO previously discussed, the core investigation of this thesis involves a quantitative comparison between representative configurations of these two orbit types. The primary goal is to evaluate and compare their mission efficiency by analyzing how effectively each orbit type balances maximum visibility opportunities for the onboard AI airplane detection task against the associated onboard energy consumption.

1.2 *Study Objectives and Methodology Overview*

The primary objective of this thesis is to quantitatively evaluate and compare the mission efficiency of representative SSO and NSSO configurations for autonomous aerial surveillance via onboard

artificial intelligence. This evaluation specifically analyzes the trade-off between maximizing target visibility opportunities and minimizing associated onboard energy consumption for the defined mission scenario.

To achieve the stated objective, this study employed a simulation-based methodology. Custom Python scripts were developed to propagate satellite orbits, incorporating J2 perturbation effects with a fixed epoch (20 March 2025), and the framework's ground track calculations were validated against General Mission Analysis Tool (GMAT) results. The performance of representative SSO and NSSO configurations targeting Incheon Airport (ICN) (minimum 20° elevation) was analyzed over both 1-day and 7-day simulation periods. Key performance metrics focused on target visibility, including pass frequency, duration, and specifically daytime access suitable for the assumed optical sensor. The evaluation specifically focuses on daytime operations, assuming only images captured during daylight hours are usable for reliable airplane detection with the specified optical sensor, thus defining a key boundary for visibility and energy consumption analyses. A composite scoring system, weighting these visibility metrics against estimated energy usage, is then proposed and implemented in order to evaluate the overall mission efficiency of each orbit configuration. The simulated onboard system reflects a power-constrained mid-size satellite platform, equipped with a KOMPSAT-3-class optical sensor and an NVIDIA Jetson Xavier NX module running an optimized YOLOv5n model for onboard airplane detection. The energy model accounts for power consumption during image acquisition, AI inference, result transmission, and standby periods, reflecting realistic subsystem demands under limited orbital power budgets.

1.3 *Thesis Roadmap*

The remainder of this thesis is structured as follows. Chapter 2 provides essential background information, covering relevant concepts in orbital mechanics, details on Sun-Synchronous and Non-Sun-Synchronous orbits, satellite systems pertinent to edge computing, and artificial intelligence algorithms for object detection, and related work in these areas.

Chapter 3 details the specific methodology employed, including the simulation setup, propagation models, visibility metrics, composite scoring approach, key parameters, and the assumptions made regarding the onboard system and energy modeling for the comparative analysis.

Chapter 4 presents the quantitative results derived from the simulations, encompassing visibility analyses, energy consumption estimates, and the efficiency scoring for the evaluated orbit configurations.

Chapter 5 discusses these results, analyzes the trade-offs between the selected SSO and NSSO representatives, draws conclusions based on the findings, and suggests potential avenues for future research.

Chapter 2

BACKGROUND

In this chapter, we discuss key principles of orbital mechanics and pertinent characteristics of satellite systems relevant to LEO missions. The discussion will also cover the fundamentals of edge computing in space applications [11] and the artificial intelligence algorithms used to detect objects onboard [14].

2.1 *Low Earth Orbit (LEO) Environment*

LEO is extensively utilized for Earth Observation (EO) and remote sensing missions, particularly those requiring high-resolution imaging of the Earth's surface. Curtis [1] defines LEO with an altitude ranging from approximately 150 km (about 100 miles) to an upper limit of about 2000 km (1200 miles). This orbital regime lies well above the drag-producing atmosphere, whose significant effects taper off around 80 km (50 miles), and remains safely below the inner Van Allen radiation belt, which begins near 2400 km (1500 miles) [1]. The proximity of LEO to Earth makes it especially favorable for applications that require high-resolution terrestrial imaging and frequent revisit opportunities.

In reality, satellite orbits deviate from ideal Keplerian motion due to various perturbative forces acting over time. For missions in LEO, the most significant perturbations arise from the Earth's oblateness—commonly referred to as the J_2 effect—and atmospheric drag. While atmospheric drag causes a gradual loss of orbital energy, particularly in lower LEO altitudes, the J_2 perturbation dominates the long-term evolution of orbital geometry for most near-circular orbits.

The Earth's equatorial bulge creates a non-spherical gravitational potential, leading to secular changes in two key orbital elements: the Right Ascension of the Ascending Node (RAAN, Ω) and the Argument of Perigee (AOP, ω) [1].

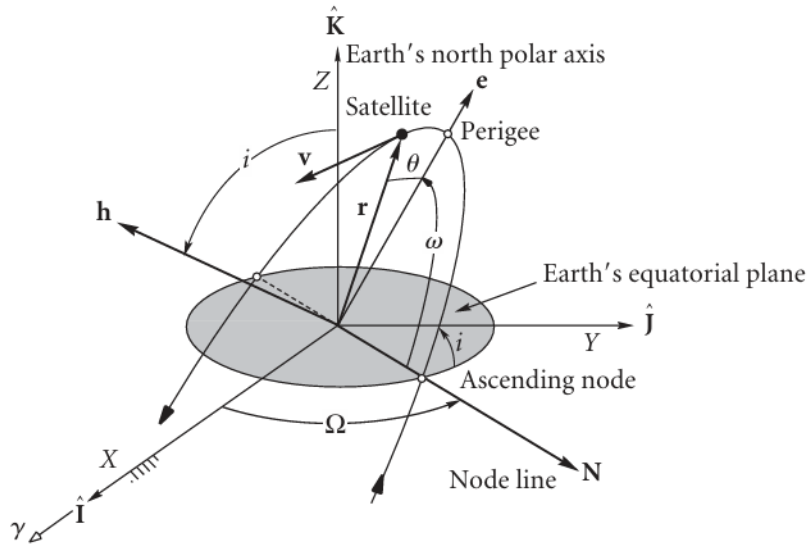

Figure 2.1: Key orbital elements: Inclination i, RAAN (Ω), and Argument of Perigee (ω) shown in an Earth-centered inertial frame [1]

The change in RAAN, known as nodal regression, describes the precession of the orbital plane about Earth's rotational axis. The change in AOP, known as apsidal precession, refers to the gradual rotation of the orbit's ellipse within the orbital plane.

The rate of nodal precession due to the J_2 term is given by:

$$\dot{\Omega} = -\left[\frac{3}{2}\frac{\sqrt{\mu}J_2R_E^2}{(1-e^2)^2a^{7/2}}\right]\cos(i) \tag{2.1}$$

Similarly, the rate of apsidal precession (rotation of the perigee) is given by:

$$\dot{\omega} = -\left[\frac{3}{2}\frac{\sqrt{\mu}J_2R_E^2}{(1-e^2)^2a^{7/2}}\right]\left(\frac{5}{2}\sin^2(i) - 2\right) \tag{2.2}$$

where:

- J_2 is the second zonal harmonic coefficient of the gravitational field of EarthEarth ($1.08263(10^{-3})$).
- R_E is Earth's equatorial radius (approximately 6378 km).

- a is the semi-major axis of the satellite's orbit.
- e is the orbital eccentricity, which measures the deviation of the orbit from being perfectly circular.
- μ is Earth's standard gravitational parameter, defined as $\mu = GM$, where G is the gravitational constant and M is the mass of the Earth. For Earth, $\mu \approx 3.986 \times 10^{14}\ \mathrm{m}^3\ \mathrm{s}^{-2}$.
- i is the inclination of the satellite's orbit, measured from the equatorial plane.

These expressions quantify how both the orbital plane and the orientation of the orbit within the plane evolve due to the Earth's oblateness. In particular, RAAN experiences retrograde motion ($\dot{\Omega} < 0$) for prograde orbits ($i < 90^\circ$).

Understanding these J_2-induced precessions is fundamental for designing orbits with consistent ground track behavior or repeat coverage patterns. For instance, some specialized orbits exploit this natural precession to maintain a fixed relationship with the Sun or to ensure stable imaging geometry over long periods. These strategies will be discussed in more detail in the following sections.

2.2 *Orbit Types for Earth Observation*(*EO*)

The interaction of satellite orbits with natural perturbations, particularly the J_2 effect discussed in Section 2.1, gives rise to distinct classes of LEOs commonly employed for EO. Selecting an appropriate orbit type involves strategically leveraging or mitigating these perturbations to achieve specific mission objectives, such as ensuring consistent observation conditions or achieving precise revisit patterns. This section will detail the two primary LEO categories pertinent to this study: SSO and NSSO. Their fundamental characteristics, as well as their respective advantages and limitations for AI-based airplane detection missions onboard, will be systematically discussed.

2.2.1 Sun-Synchronous Orbits (SSO)

(1) General Characteristics

SSO is a specialized type of LEO that maintains a consistent angle α between its orbital plane and the direction of sunlight, as illustrated in Figure 2.2.

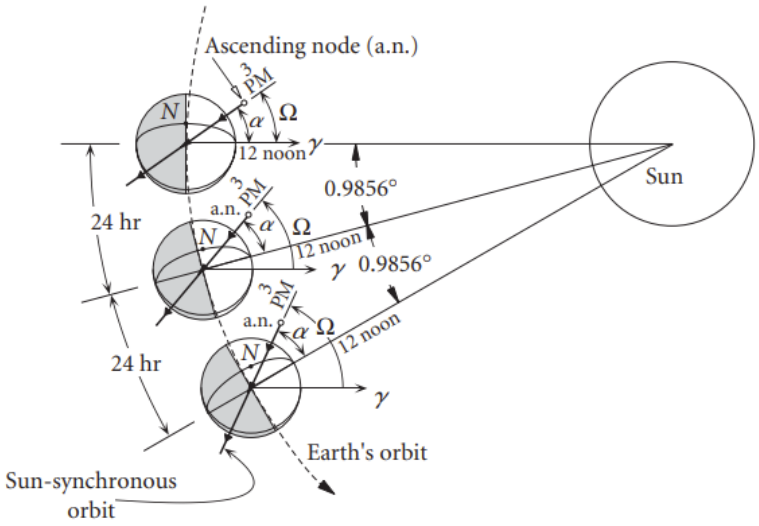

Figure 2.2: Illustration of a SSO [1]

This Sun-synchronous condition is typically achieved by selecting a specific orbital inclination, usually between 97.3° and 98.1° for altitudes ranging from 600 to 800 km—that allows the orbital plane to precess at the same rate as the Earth's revolution around the Sun [12]. This range is commonly used in EO satellites for its practical balance between coverage and the frequency of re-visitation.

In Figure 2.2, we view the Earth from above the North Pole. Earth orbits the Sun in a counterclockwise direction, with the Vernal Equinox (γ) serving as a fixed inertial reference point. The angle Ω, known as the right ascending node (RAAN), is measured eastward from this direction to the point where the satellite's orbit crosses the equator moving northward [1]. For an orbit to be Sun-synchronous, the RAAN accelerates eastward at approximately 0.9856° per day, matching Earth's mean orbital progression around the Sun [1]. Such an orbital alignment enables satellites to observe Earth under similar lighting conditions each day, thereby stabilizing the local solar time across overpasses.

(2) Advantages and Limitations of SSO

One key advantage of SSO is its ability to collect images under consistent solar illumination, typically during optimal local times [1, 12, 13]. This consistency in illumination not only improves image quality for visual assessment [15, 16], but also simplifies the operational conditions for the YOLOv5n model on board [11, 14]. By minimizing ambiguities caused by varying shadows or glare, the AI model can achieve more reliable detection performance [14, 17]. Furthermore, predictable lighting can reduce the complexity of image pre-processing algorithms executed on the Jetson Xavier NX. As a result, the system uses energy more efficiently per inference task during daytime passes over ICN. [5].

However, fixed MLST introduces limitations, particularly in terms of observation scheduling and revisit flexibility for dynamic targets, such as airports. For a dynamic target environment like Incheon International Airport, where airplane movements and operational tempo vary significantly throughout the day, the rigid revisit schedule of an SSO means that critical activities occurring outside the fixed MLST pass window will be systematically unobserved. This inherent limitation can hinder the ability to detect unscheduled or transient aeronautical events and to build a comprehensive operational picture [18]. Consequently, while each SSO image benefits from consistent illumination, the overall effectiveness of surveillance for time-critical airplane detection tasks at ICN might be constrained, potentially leading to a higher energy cost per relevant detection compared to NSSOs that could offer more frequent, though variably illuminated, observation opportunities throughout the day [15].

(2) Designing a Sun-Synchronous Orbit (SSO)

Designing a SSO involves ensuring that the satellite's Right Ascension of the Ascending Node (RAAN) precesses at a rate matching the Earth's average orbital motion around the Sun. This rate is approximately:

$$\dot{\Omega}_{SSO} = \frac{2\pi \text{ rad}}{365.26 \times 24 \times 3600 \text{ s}} = 1.991 \times 10^{-7} \text{ rad/s}$$

Although this precession rate is often stated as 0.9856° per day, it is more precise to use the radian value for calculation consistency. This conversion is calculated as:

$$0.9856^\circ \times \frac{\pi \text{ rad}}{180^\circ} = 0.0172 \text{ rad/day}$$

$$0.0172 \text{ rad/day} \times \frac{1 \text{ day}}{86400 \text{ s}} = 1.991 \times 10^{-7} \text{ rad/s}$$

The J2 precession equation, already derived in Section 2.1 (Equation 2.1), describes how the RAAN of an orbit evolves over time due to the Earth's oblateness. For convenience, this equation is recalled here:

$$\dot{\Omega} = -\left[\frac{3}{2}\frac{\sqrt{\mu}J_2R_E^2}{(1-e^2)^2a^{7/2}}\right]\cos(i)$$

In this study, since we are assuming the use of Komsat-3's optical system, the design objective is to maintain an SSO at an altitude of 687 km. Given this altitude, the semi-major axis becomes:

$$a = R_E + z = 6371 \text{ km} + 687 \text{ km} = 7058 \text{ km}$$

The eccentricity of the orbit is set to $e = 0.0001$ instead of assuming a perfectly circular orbit ($e = 0$). This slight eccentricity is introduced to add a touch of realism to the calculation, reflecting the fact that even carefully designed SSOs are rarely perfectly circular.

Substituting the values into the J2 precession equation for the required SSO precession rate of $\dot{\Omega} = 1.991 \times 10^{-7}$ rad/s, we have:

$$1.991 \times 10^{-7} = -\frac{3}{2}\frac{\sqrt{\mu}J_2R_E^2}{(1-e^2)^2a^{7/2}}\cos(i)$$

Plugging in the orbital parameters:

$$1.991 \times 10^{-7} = -\left[\frac{3}{2}\frac{\sqrt{3.986 \times 10^{14} \text{ m}^3 \text{ s}^{-2}} \times (1.08263 \times 10^{-3}) \times (6371 \times 10^3 \text{ m})^2}{(1-(0.0001)^2)^2 \times (7058 \times 10^3 \text{ m})^{7/2}}\right]\cos(i)$$

Thus, the inclination of the orbit is calculated as:

$$\cos(i) = -0.13989$$

$$i = \arccos(-0.13989) \approx 98.12^\circ$$

2.2.2 Non-Sun-Synchronous Orbits (NSSO)

(1) General Characteristics

NSSOs are orbits that do not maintain the defining characteristics of SSOs. In NSSOs, the angle between the orbital plane and the Sun is not constant, causing the Mean Local Solar Time (MLST) of ground passes to vary over time. This variation occurs because these orbits fall outside the inclination conditions required to maintain sun-synchronicity and are therefore categorized as NSSOs. Since NSSOs do not have fixed MLST, the revisit time of satellites on the orbits will continuously change. This means that the satellites will have the Earth's image in different lighting conditions [1].

(2) Advantages and Limitations of NSSO

NSSOs offer notable advantages in terms of both temporal and spatial flexibility. Unlike SSOs, which require near-polar inclinations to maintain sun-synchronicity, NSSOs allow a wider range of inclination angles, enabling mission designers to tailor orbits for prolonged coverage over specific regions. Additionally, the absence of a fixed Mean Local Solar Time (MLST) provides access to diverse observation times throughout the day, improving revisit frequency and reducing the risk of missing time-sensitive or transient events [15]. This makes NSSOs particularly suitable for dynamic monitoring tasks, such as airport surveillance or disaster response [3, 15, 18].

Despite their flexibility, NSSOs present several limitations, particularly in the context of optical Earth observation. Varying illumination conditions across passes can result in inconsistent image quality due to shifts in glare, shadow, and contrast [9]. This variability complicates image interpretation and demands more robust cite s24134098, s22031147, LinHao2024ASoD, often energy-intensive AI models to compensate for input variability to ensure reliable performance across changing inputs [11, 5]. Moreover, the lack of predictable solar exposure may hinder power planning, as satellites cannot rely on consistent sunlight during every orbit, posing challenges for energy-constrained platforms cite duggan2025advancingearthobservationsurvey.

(3) NSSO Configuration Parameters and General Design Considerations

While the previous sections have outlined the general characteristics and trade-offs associated with NSSOs, this study investigates explicitly how varying key NSSO orbital parameters can influence

mission effectiveness for the defined airplane surveillance task in a specific region. The primary motivation for exploring a range of NSSO configurations is to move beyond the observational constraints of a traditional SSO, particularly its fixed MLST for target passes.

This research will systematically vary fundamental NSSO design parameters, including **orbital inclination**, **Right Ascension of the Ascending Node (RAAN)**, and **Argument of Perigee (AOP)**, across a predefined set of values. The objective is to quantitatively assess the impact of these variations on critical performance metrics, namely the visibility opportunities over Incheon Airport (ICN) suitable for optical airplane detection, and the associated onboard energy consumption.

By simulating and analyzing a diverse set of NSSOs, this study aims to identify orbital configurations that may offer a more advantageous balance between maximizing useful, daylight observation passes and minimizing energy expenditure compared to a baseline SSO. The specific ranges for these parameters, the rationale for their selection, and the detailed simulation methodology employed for this comparative analysis will be elaborated in Chapter 3 (Methodology). This approach will allow for a focused examination of how NSSO design flexibility can be leveraged to enhance the efficiency of LEO satellite edge computing missions for responsive surveillance.

2.3 *Satellite Visibility*

For the primary objective of this study, which is to detect airplanes using an onboard AI system, it is essential to assess when and how the satellite has visibility of the target on the ground, specifically Incheon International Airport (ICN). Satellite visibility, in this context, refers to the periods during which a direct line of sight exists between the satellite and the ICN, under conditions suitable for practical observation by the onboard optical sensor.

A fundamental concept for determining visibility is the **elevation angle**. This is defined as the angle measured upward from the local horizon at the ICN to the satellite's position in the sky. The elevation angle is significant for several reasons. Firstly, a sufficiently high elevation angle is necessary to avoid line-of-sight obstructions from terrain or tall structures; however, this is less of a concern in an open environment like ICN. Secondly, a higher elevation angle generally corresponds to a shorter atmospheric path length for the sensor's line of sight, which can reduce atmospheric distortion and improve image quality.

Although high-resolution EO missions typically favor elevation angles in the $50°$–$60°$ range—such as the case with KOMPSAT-3—to achieve optimal spatial clarity and geometric fidelity [19], this study employs a more relaxed minimum elevation threshold of $20°$. Given that the target environment (ICN) is relatively flat and unobstructed, such off-nadir observations remain operationally feasible. The technical rationale for this threshold, including relevant capabilities of satellite sensors, is discussed in detail in the methodology section. A **satellite pass** is thus defined as a continuous period during which the satellite remains above this $20°$ minimum elevation threshold as viewed from the ICN.

Ground Sample Distance (GSD) and Viewing Geometry

The elevation angle also has significant geometric consequences for image acquisition. As the elevation angle decreases (for more oblique, off-nadir viewing), the **slant range**—the direct line-of-sight distance between the satellite and the ground target – increases relative to the vertical altitude of the satellite. This extended slant range leads to a larger imaging footprint on the ground and, consequently, a degradation in spatial resolution.

In optical remote sensing, spatial resolution is typically characterized by the GSD, which approximates the ground-projected size of a single detector pixel. For nadir viewing geometry, the GSD is derived from the principle of similar triangles between the detector array and the projected ground footprint. The theoretical model assumes the imaging geometry shown in Figure 2.3, where the flying height above ground is measured from the focal point of the lens [2]. This yields the expression:

$$\text{GSD} = \frac{H' \cdot p}{f} \tag{2.3}$$

Where H' is the distance from the focal point to the ground, p is the physical size of a detector pixel element, and f is the focal length of the optical system.

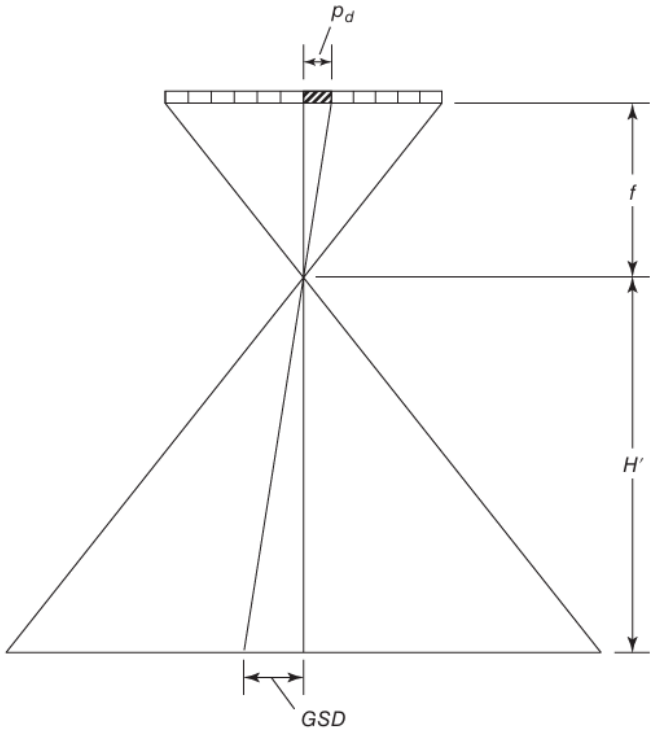

Figure 2.3: Geometric derivation of GSD using similar triangles [2]

As shown in Figure 2.3, this derivation is based on the formulation discussed by Lillesand et al. [2].

In orbital imaging scenarios, it is common to approximate the satellite imaging altitude H as the total distance from the satellite body (sensor assembly) to the ground, such that $H \approx H' + f$. Given that $f \ll H$, this approximation introduces negligible error. Therefore, Equation 2.3 can be practically rewritten as:

$$\text{GSD} \approx \frac{H \cdot p}{f} \tag{2.4}$$

For off-nadir viewing, the slant range R replaces the vertical altitude H in this relationship:

$$\text{GSD} \approx \frac{R \cdot p}{f} \tag{2.5}$$

Since $R > H$ for any off-nadir angle, the GSD increases with decreasing elevation angle, leading

to reduced spatial detail. This geometric relationship is illustrated in Figure 2.4. This inherent trade-off underscores the importance of carefully selecting the minimum elevation threshold and orbital parameters to satisfy resolution requirements for tasks such as object detection.

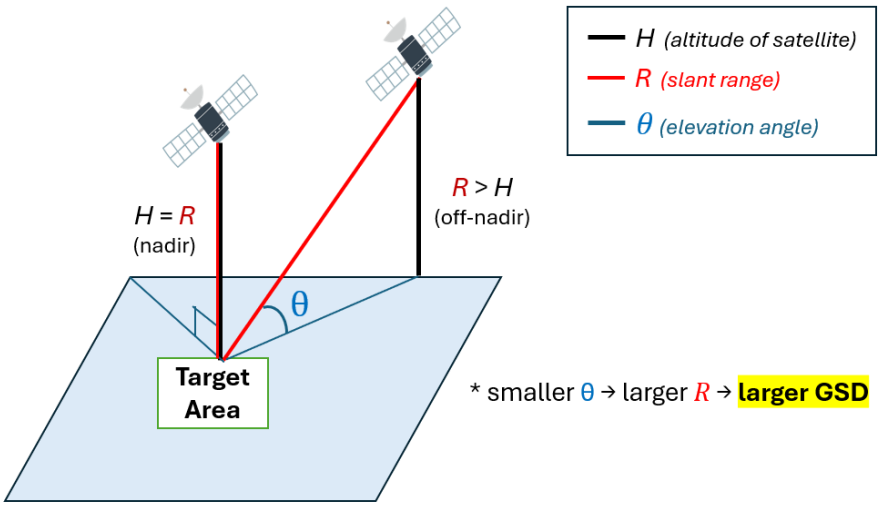

Figure 2.4: Geometry of nadir vs. off-nadir imaging in satellite-based EO. As the elevation angle θ decreases, the slant range R increases relative to the altitude H, resulting in a larger GSD and reduced spatial resolution.

Therefore, careful planning of the satellite's orbital altitude is critical to ensure the resulting GSD and overall image clarity are adequate for the AI model to detect airplanes [12, 14] reliably. Other orbital parameters, such as **inclination** and the **target's latitude**, also inherently influence the geometry and frequency of visibility opportunities [1]. In contrast, the **sensor's characteristics** (e.g., field of view, focal length) dictate the observable area (swath width) and the achievable resolution from a given orbit [20].

To quantify and compare the visibility afforded by different orbital configurations, this study will use three key metrics:

1. **Maximum Single Pass Duration (`max_pass_duration`):** This metric records the most extended continuous duration of any single valid observation pass over the target. It highlights the

potential for extended, uninterrupted observation during a flyover, which can be advantageous for acquiring higher-quality data or performing more detailed analysis.

2. **Total Visible Duration (`total_visible_duration`):** This represents the cumulative sum of the durations of all valid passes over the simulation period. It underscores the overall visibility time an orbit provides to the target, reflecting the total potential observation window.

3. **Number of Passes (`num_passes`):** This metric counts the total number of distinct valid observation passes. While revisit frequency is an essential aspect of satellite surveillance, this study focuses on the number of discrete visibility opportunities, as preliminary analyses suggested that for the short-term evaluation periods considered, pass count and duration metrics offer a more apparent distinction between the performance of different orbits.

2.4 *Edge Computing for Space Applications*

Edge computing, in the context of space applications, refers to the capability of satellites to perform data processing directly onboard the spacecraft, rather than transmitting raw sensor data to the ground stations for analysis [11]. This paradigm shifts significant computational tasks, such as airplane detection addressed in this study, from terrestrial systems to the satellite's processing hardware. After onboard analysis, only the refined information or critical results are downlinked to ground stations [4].

As satellites are increasingly tasked with real-time monitoring of dynamic targets—such as airplanes, ships, or natural disasters—the traditional model of centralized, ground-based processing is proving inadequate [3]. The growing demand for faster decision-making, low-latency responsiveness times, and operational autonomy in EO missions has accelerated the shift toward onboard intelligence. In this context, edge computing is no longer a luxury but an operational necessity for next-generation satellite systems [21].

Traditionally, satellites undertaking tasks such as airplane detection would capture imagery and transmit the entire raw dataset to ground stations, as onboard processing capabilities were limited. This approach, however, presents significant challenges: raw data volumes are often substantial, making data transmission to ground stations a burdensome process. Such heavy downlinks can

lead to considerable time latency in receiving actionable information and result in inefficient energy consumption, potentially impacting the operational lifespan of power-constrained satellites [4].

The adoption of onboard edge computing directly addresses these limitations, offering several key advantages for satellite missions. A primary motivation is the significant reduction in data downlink volume, as only processed results or essential information need to be transmitted, alleviating the strain on communication channels. This, in turn, lowers latency and enables faster responses to time-sensitive events, as analysis occurs closer to the point of data acquisition. Furthermore, by minimizing downlink requirements and optimizing data handling, edge computing can contribute to more efficient energy utilization, potentially extending the satellite's operational lifespan [4]. Onboard processing capabilities also pave the way for increased satellite autonomy, enabling AI-driven analysis using systems like the NVIDIA Jetson Xavier NX without direct human intervention from the ground. This shift is visually summarized in Figure 2.5.

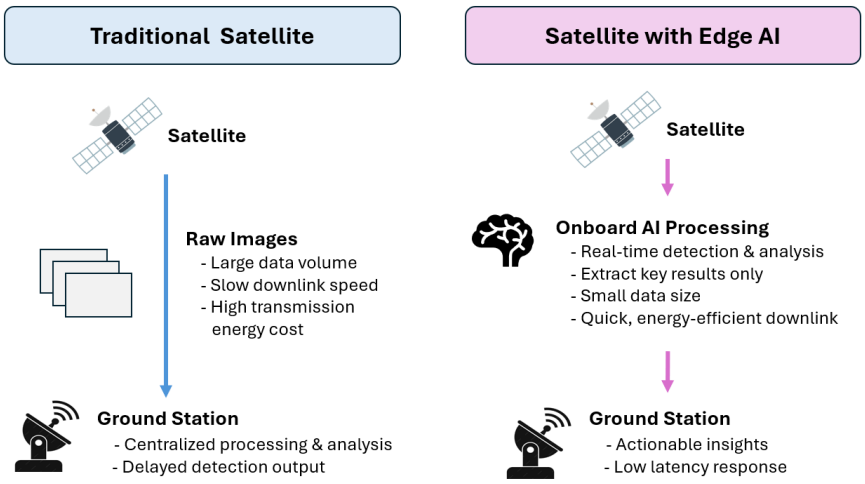

Figure 2.5: Traditional Satellite Processing vs. Satellite with Onboard Edge AI

LEO operating imposes several hardware-level constraints for AI processing systems on board. Among these, the most prominent are limitations in Size, Weight, and Power (SWaP), along with challenges in thermal management due to restricted heat dissipation capabilities in space. Although the radiation environment in LEO can affect electronic systems, and thermal management presents

significant challenges for onboard processing units [21, 22], this study does not explicitly model radiation effects, shielding, or detailed thermal dissipation strategies. Instead, it focuses on the trade-offs in energy efficiency and visibility under nominal operational conditions, assuming that basic thermal and radiation considerations for component survival and operation are met by the notional satellite platform design.

The selection of onboard processing hardware was driven by the trade-off between computational performance and the strict Size, Weight, and Power (SWaP) constraints inherent to satellite platforms. Given these constraints, compact and energy-efficient hardware platforms are essential for practical deployment. Devices such as field-programmable gate arrays (FPGAs), specialized AI accelerators, and low-power processors are commonly considered [21, 23].

Within this landscape, the NVIDIA Jetson family offers a range of options suitable for edge AI. For this study, the Jetson Xavier NX was identified as the optimal choice, representing a practical middle ground that balances performance with the mission's operational constraints.This balance becomes clear when comparing the Xavier NX to other modules in the Jetson family. The Jetson Nano, while highly power efficient, lacks the necessary processing power (up to 0.5 TFLOPS) and memory to effectively run advanced object detection models like YOLOv5n in a time-sensitive manner [24]. In contrast, the more powerful Jetson AGX Xavier, which delivers up to 32 TOPS, presents significant SWaP challenges. It operates in a larger power envelope (10-30 W) and is physically much larger (100mm x 87mm) than the NX module, making it less suitable for a satellite with a limited power and volume [25].

The Jetson Xavier NX, therefore, delivers substantial AI performance (up to 21 TOPS) within a moderate power budget (10-20 W) and, crucially, in a much more compact form factor (70mm x 45mm). This superior performance per watt and performance per volume make it the most suitable candidate for real-time inference tasks in space-constrained environments [25].

This study pairs the Jetson Xavier NX with the YOLOv5n object detection model, whose compact architecture and low latency performance make it well suited for embedded AI inference in orbit [26]. A detailed rationale for this selection is provided in Section 2.6. Given this hardware-software pairing, the next step is to evaluate whether such a configuration can operate sustainably under orbital energy constraints—a question addressed through the energy modeling framework presented in the following section.

2.5 *Energy Modeling*

This section outlines the energy modeling framework used to evaluate the sustainability of onboard AI inference operations. Both visibility opportunities and power constraints are jointly considered to derive a composite efficiency score for each orbital configuration.

2.5.1 Solar Energy Generation Model

To estimate the satellite's ability to generate power, the simulation calculates solar input based on its relative orientation with respect to the Sun at each timestep. The satellite is assumed to have four lateral body-mounted solar panels (+X, -X, +Y, -Y), while the +Z and –Z surfaces are excluded due to their typical usage for imaging sensors, antennas, or star trackers.

At every timestep, the solar irradiance incident on each panel is computed using the cosine of the angle between the Sun vector and the surface normal of the panel. Only panels facing within 90° of the Sun direction are considered active contributors to power generation.

2.5.2 Solar Vector Computation and Reference Frames

To determine the Sun's direction in space, the simulation uses a simplified solar ephemeris model based on the current day of year. First, the Sun's position is calculated in the **ecliptic frame**, which assumes that the Sun moves along a fixed orbital plane (the ecliptic) as Earth revolves around it [1].

The Sun's mean anomaly $M_\odot$ is used to estimate its position along the orbit, incorporating a correction for orbital eccentricity. This yields the Sun's ecliptic longitude $\lambda_\odot$, which defines its location along the ecliptic. From this, a unit vector is constructed in the ecliptic frame:

$$\vec{s}_{\text{ecliptic}} = \begin{bmatrix} \cos\lambda_\odot \\ \sin\lambda_\odot \\ 0 \end{bmatrix}$$

Since the rest of the simulation is conducted in the Earth-Centered Inertial (ECI) frame, the Sun vector must be rotated accordingly. This is done by applying a rotation of $\epsilon \approx 23.44^\circ$, which accounts for Earth's axial tilt:

$$\vec{s}_{\text{ECI}} = R_x(\epsilon) \cdot \vec{s}_{\text{ecliptic}}$$

Here, $R_x(\epsilon)$ is the standard rotation matrix about the x-axis. The result, $\vec{s}_{\text{ECI}}$, gives the Sun's direction in the ECI frame and is used throughout the simulation to determine if the satellite is illuminated.

2.5.3 Satellite Body Frame Definition

To accurately compute solar exposure on each body-mounted panel, the satellite's orientation must be defined in a valid, orthonormal reference frame. While full attitude dynamics are not modeled, the simulation adopts a standard orbital-based frame often referred to as the Local Vertical Local Horizontal (LVLH) frame [1]:

- The $+\hat{z}_{\text{body}}$ axis points toward Earth's center: $\hat{z} = -\vec{R}/|\vec{R}|$,
- The $+\hat{y}_{\text{body}}$ axis is perpendicular to the orbital plane (anti-orbital momentum): $\hat{y} = -(\vec{R} \times \vec{V})/|\vec{R} \times \vec{V}|$,
- The $+\hat{x}_{\text{body}}$ axis completes the right-handed system: $\hat{x} = \hat{y} \times \hat{z}$.

This orthonormal body frame ensures consistent geometric interpretation at all timesteps, even in slightly elliptical orbits. The Sun vector, initially expressed in ECI coordinates, is transformed into this body frame using dot products with each basis vector. These projections are then used to evaluate the angle of incidence on each solar panel surface.

2.5.4 Energy Consumption Model

To assess the operational viability of each orbit, a power budget model is simulated to track energy consumption over time. This model is critical for determining whether the onboard systems—particularly the power-intensive AI processor—can be sustainably operated. The satellite's power draw is categorized into two distinct operational modes: a high-consumption **active mode** during target observation and a baseline **standby mode** for all other periods.

- **Active Mode:** This mode encompasses the full operational sequence required for an intelligent detection pass: image acquisition, onboard data processing, and the subsequent transmission of results. The energy for each component is modeled on the basis of realistic performance benchmarks for satellite hardware [25].

  – *Image Capture* (P_{capture}, t_{capture}): Represents the power draw of the optical payload during image acquisition.

  – *AI Inference* (P_{process}, $t_{\text{process\_per\_tile}}$): This is the core energy cost of the edge computing paradigm. It models the power consumed by the Jetson Xavier NX to execute the YOLOv5n algorithm on each image tile [25].

  – *Transmission* (P_{tx}, t_{tx}): Represents the energy required to downlink the compact results (i.e., detection coordinates), not the raw image, which is consistent with the benefits of onboard processing.

The total energy for processing a single image strip is therefore the sum of these components:

$$E_{\text{active\_strip}} = E_{\text{capture}} + (N_{\text{tiles}} \cdot E_{\text{process\_per\_tile}}) + E_{\text{tx}}$$

– E_{capture}: The energy required to capture an image strip using the satellite's optical payload, camera. It is calculated as the product of the sensor's power draw and the capture time [27, 28].

– N_{tiles}: The total number of image tiles extracted from a single image strip. Each tile is processed individually by the onboard AI model, and this number is determined by the sensor resolution, tile size, and overlap settings.

– $E_{\text{process\_per\_tile}}$: The energy required to perform object detection on one tile using the YOLOv5n model running on the Jetson Xavier NX. This accounts for the power usage and processing time for a single tile inference [25].

– E_{tx}: The energy used to transmit the inference results (i.e., detection metadata such as bounding box coordinates) back to the ground station. Since only compact results are sent—not the full image—the energy consumption is relatively small but still included for completeness.

2.5.5 Energy Balance and Composite Score

The **net energy balance** is the difference between energy generated and energy consumed:

$$E_{\text{net}} = E_{\text{generated}} - E_{\text{consumed}}$$

This quantity indicates whether a particular orbit can sustain continuous AI operations over time. To holistically evaluate orbital configurations, this value is combined with visibility metrics, such as the number of valid passes, total visible time, and maximum pass duration, into a composite efficiency score. Each component is normalized and equally weighted to yield a final ranking across candidate orbits.

2.6 *Object Detection with Deep Learning*

Object detection stands as a critical task within computer vision, focusing on the precise localization and classification of specific targets within an image. In the context of EO, this capability is invaluable for applications ranging from monitoring topographical changes to tracking the movement of vehicles such as ships, cars, and airplanes [11, 14]. Satellite-based optical sensors capture imagery of the Earth's surface, and with the advent of onboard processing, computational systems on the satellite can analyze these images to identify objects of interest and determine their coordinates [21, 5].

However, detecting objects from satellite imagery presents some challenges. The significant distance between the satellite and the Earth's surface can result in images with inherently lower spatial resolution (larger Ground Sample Distance) compared to terrestrial or aerial photography, making it difficult to discern small objects [2]. Furthermore, variations in illumination due to factors such as time of day, weather conditions, or shadows can further complicate image interpretation and object identification [17, 14], as shown in Figure 2.6. Figure 2.6 illustrates how environmental conditions such as cloud cover, shadows, and varying solar angles can degrade the visual clarity and reliability of object detection in satellite imagery. The images were created by the author based on optical satellite data from the *HRPlanesv2* dataset [29], with additional brightness and contrast adjustments to simulate diverse atmospheric and lighting scenarios.

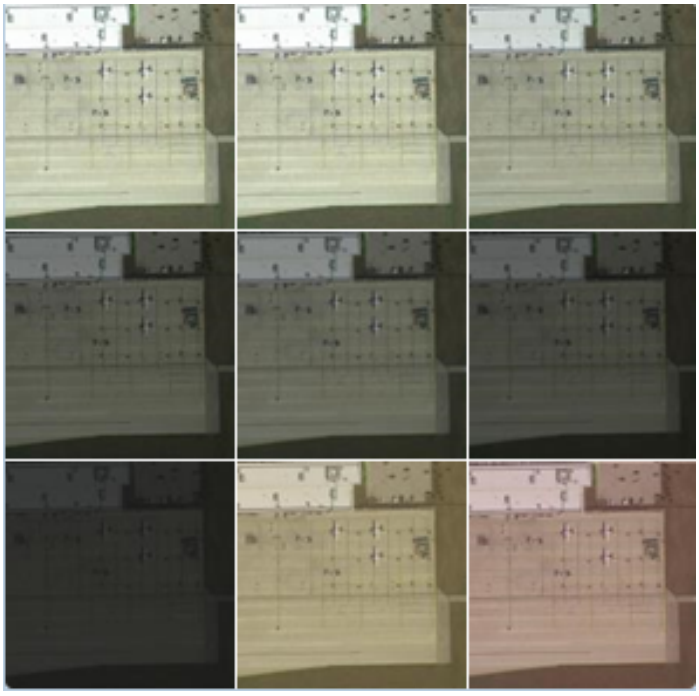

Figure 2.6: Satellite imagery under varying weather and illumination conditions affecting object detection

To address these limitations and enhance the capabilities of object detection from satellite imagery, deep learning methodologies, particularly Convolutional Neural Networks (CNNs), have become increasingly prominent [30, 31]. CNNs are useful for image analysis tasks as they can automatically learn hierarchical features, from simple edges and textures to complex object parts and complete objects, directly from large datasets. Through extensive training, these networks learn to identify the characteristic patterns and shapes associated with specific target classes.

Among the various deep learning architectures for object detection, the You Only Look Once (YOLO) family of models has gained widespread recognition [32]. YOLO models are one-stage detectors that perform object localization and classification in a single pass through the network. This contributes to their notable processing speed, making them suitable for real-time or near-real-time applications. YOLOv5, a specific iteration within this family, offers several variants that balance model size, speed, and accuracy. For deployment on power-constrained edge devices in space environments, lightweight versions such as YOLOv5n are particularly relevant due to their reduced

computational footprint and parameter count, while still offering acceptable detection performance [26]. This study adopts YOLOv5n as the primary detection model due to its balance between inference efficiency and suitability for mid-size satellite platforms operating under limited power budgets.

To demonstrate the object detection capability of YOLOv5n in satellite imagery, a series of inference tests was conducted using high-resolution images from the *HRPlanesv2* dataset. The

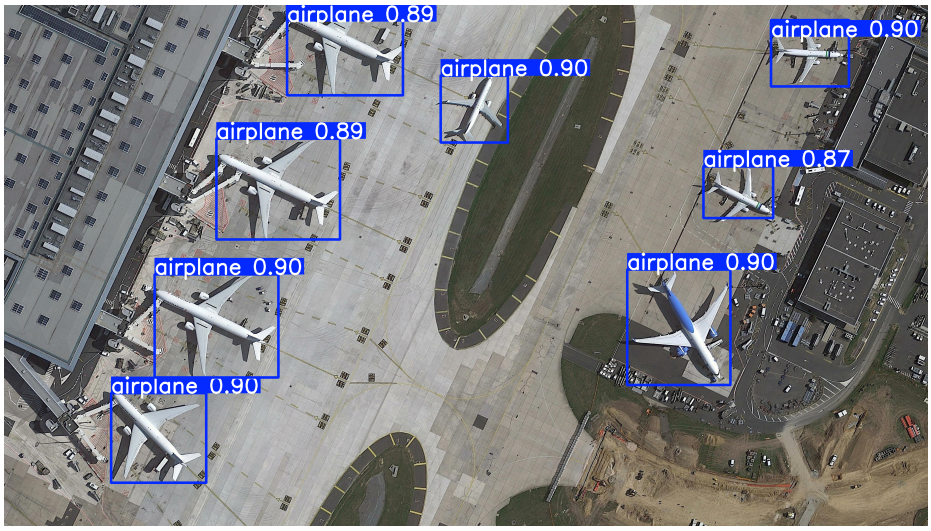

Figure 2.7: YOLOv5n detection output showing airplanes' bounding boxes in satellite imagery

detection results shown in Figure 2.7 were produced using a custom inference pipeline implemented by the author. Although the underlying image was sourced from the *HRPlanesv2* dataset [29], all stages of model execution, including preprocessing, visualization of the bounding box, and export of results, were independently handled as part of the simulation workflow of this study.

2.6.1 Operational Implications of YOLOv5n Selection

While the YOLOv5n model was not directly executed on actual Jetson Xavier NX hardware in this study, its selection is grounded in prior benchmarks and well-documented performance characteristics [26]. Due to the unavailability of real hardware and the impracticality of replicating a fully accurate onboard simulation environment, real-time inference was not incorporated into the

simulation pipeline. Nonetheless, the selection of YOLOv5n reflects realistic deployment considerations, and its computational profile informs key assumptions within the energy and orbital visibility analysis[25].

Daylight Dependence and Illumination Assumptions: Optical object detection models such as YOLOv5n are known to be sensitive to ambient lighting conditions[17]. However, this study does not empirically evaluate detection performance across varying illumination scenarios (e.g., shadowing, cloud cover, low-angle sunlight), as realistic environmental variation is difficult to replicate reliably in simulation. Instead, we conservatively restrict valid inference to daytime passes, assuming **clear-sky and nominal sunlit conditions throughout**. This simplification avoids speculative augmentation and ensures consistency with the behavior of the model as compared to well-lit imagery [17]. It also implies that all daytime imagery is treated as suitable for detection, despite the potential presence of weather-induced degradation in real-world missions. Consequently, orbit selection and visibility analysis in this study were driven by the quantity and quality of such daytime opportunities.

Minimum Elevation Threshold: The detection performance of YOLOv5n, like other object detection models, is heavily influenced by image quality - specifically the GSD [17], which determines spatial resolution. GSD increases as the satellite observes the target from lower elevation angles due to a longer slant range [2]. This results in coarser imagery, where small objects such as airplanes become harder to distinguish from the background. In particular, airplane detection relies on identifying fine features like wings and fuselage shape, which can be lost or distorted at lower resolutions [17].

Although this study does not empirically quantify YOLOv5n's performance degradation at varying GSDs, established literature and detection benchmarks consistently show that small object detection accuracy drops sharply once resolution falls below a certain threshold [17]. Based on this understanding, a conservative minimum elevation angle of 20° was adopted in the simulation. At this angle, the corresponding off-nadir GSD remains within an acceptable range for YOLOv5n to detect airplanes with reasonable accuracy, balancing both spatial clarity and access duration [33, 27, 28].

This elevation constraint serves two purposes. First, it ensures that only imagery with sufficient resolution is considered for inference, maintaining realistic detection outcomes and avoiding inflated visibility counts from poor-quality data [17]. Second, it is tightly integrated with the energy model: lower-quality images may lead to longer processing times, increased false positives, or failed detections—all of which can increase energy consumption per tile [5]. By filtering out suboptimal passes, the simulation preserves both inference efficiency and the validity of energy estimates.

Hardware Feasibility and Model Selection: The selection of an appropriate AI model is not made in isolation; it is fundamentally constrained by the capabilities of the onboard processing hardware. For this study, the NVIDIA Jetson Xavier NX was chosen as a representative edge computing platform, offering a strong balance between computational performance and the strict Size, Weight, and Power (SWaP) limitations inherent to satellite missions [21]. Consequently, the object detection model must be carefully selected to operate efficiently within the performance envelope of this specific hardware.

While the YOLOv5 family offers several variants (e.g., s, m, l, x) that provide progressively higher detection accuracy, this increased performance comes at the cost of significantly greater computational complexity and power consumption. Larger models would exceed the sustainable capacity of the Jetson Xavier NX in a constrained space environment [25].

Therefore, the YOLOv5n (nano) variant was specifically chosen. Its lightweight architecture is explicitly designed for high-efficiency inference on resource-constrained edge devices [26]. More importantly, recent comparative studies on satellite imagery have demonstrated that YOLOv5n exhibits outstanding performance specifically for aircraft detection tasks, making it an ideal candidate for this mission context [7]. This pairing was essential for modeling a realistic onboard system. The energy model's key parameters—namely the processing power (P_{process}) and the per-tile inference time ($t_{\text{process\_per\_tile}}$)—were adopted from published benchmarks of YOLOv5n executed on the Xavier NX [5]. As such, the computational and energy estimates used in this thesis are not hypothetical; they are firmly grounded in the empirical performance data for the selected model-hardware combination.

2.7 *Related Work*

Understanding the context and limitations of existing approaches is crucial to identifying the value and novelty of this study. This section surveys prior work in three key areas that intersect with this thesis: first, the trade-offs between SSOs and NSSOs for EO missions; second, the rise of edge AI and onboard processing in satellite systems; and third, the evolution of object detection techniques in satellite imagery, particularly for detecting aircraft. Each subsection highlights both progress and persistent gaps, leading to a clearer description of the contribution of this thesis.

2.7.1 Orbital Configuration Comparisons

Several studies have explored the suitability of various orbital configurations for EO tasks, with SSOs often preferred due to their consistent lighting conditions and near-global coverage. These orbits provide uniform solar illumination across revisits, which simplifies image interpretation and reduces the computational burden on onboard inference systems [1, 12, 13, 34], .

However, the fixed Mean Local Solar Time (MLST) of SSOs imposes temporal constraints that may not align with mission-specific visibility windows or optimal illumination for dynamic target detection, such as aircraft. To address this rigidity, recent studies have investigated inclined and NSSOs, which decouple revisit timing from solar geometry. For instance, Thapa et al. simulated inclined orbit constellations and demonstrated an increased revisit frequency over regions of interest by relaxing the strict MLST constraint [15]. These results suggest that NSSOs could enable greater operational flexibility, particularly when paired with onboard processing and dynamic scheduling.

Despite these advances, few studies have explicitly quantified the trade-offs between SSO and NSSO configurations in terms of onboard energy consumption and detection performance. This thesis contributes to this underexplored area by evaluating how variations in orbital inclination and RAAN influence daylight availability, inference opportunity, and the resulting energy efficiency of deep learning-based object detection pipelines on power-constrained mid-size satellite platforms.

2.7.2 Edge AI and Onboard Processing on Satellites

Recent advances in satellite computing hardware have enabled the integration of edge AI capabilities, allowing inference tasks to be performed onboard rather than relaying all raw data to ground stations.

This shift is critical for missions constrained by limited downlink bandwidth, latency requirements, or a need for real-time response [4, 11].

Several studies have demonstrated the feasibility of onboard inference. Veyette et al. [21] and Bayer et al. [5] present frameworks for deploying machine learning models directly on mid-size satellite platforms, utilizing optimized neural networks and specialized hardware like AI accelerators or FPGAs. Shen et al. [6] implement a multi-class object detection pipeline onboard, achieving high accuracy for geospatial targets across multiple classes. The increasing availability of platforms such as NVIDIA Jetson or Intel Movidius for aerospace use has also encouraged experimentation in this space, despite concerns about radiation tolerance and thermal constraints [22, 35].

Yet, much of the existing work either assumes fixed orbital parameters (often SSO) or evaluates model performance in static simulation environments. There remains a lack of studies that evaluate how orbital dynamics, such as inclination or RAAN, interact with the timing and energy requirements of onboard inference tasks. This thesis addresses that gap by simulating deep learning-based object detection pipelines across a diverse set of orbital configurations, with a focus on power availability and illumination scheduling.

2.7.3 Object Detection from Satellite Imagery

Object detection in satellite imagery is a well-established research area in remote sensing and computer vision. Traditional approaches relied on hand-crafted features and classical machine learning models, which were often sensitive to noise, lighting variations, and scale differences. With the advent of deep learning, particularly Convolutional Neural Networks (CNNs), performance has improved dramatically [30, 31]. Recent work has shown that CNN-based models can robustly detect various classes of objects, including buildings, vehicles, and aircraft, even in complex backgrounds and under challenging imaging conditions [14, 7].

Aircraft detection, in particular, has received growing attention due to its relevance in both civil and defense applications. Van Etten et al. [3] demonstrated the feasibility of detecting airplanes on a global scale using daily PlanetScope images. Similarly, El Ghazouali et al. conducted a comparative study of detection algorithms on high-resolution satellite imagery and reported that deep learning-based models, including YOLO and RetinaNet variants, significantly outperformed

traditional techniques [7].

While many of these studies report promising detection accuracy, they often assume idealized conditions such as fixed viewing geometries, unconstrained power availability, or post-processing on the ground. Few works have addressed the challenges of conducting inference directly onboard satellites, especially in terms of energy constraints, daylight availability, and orbital visibility windows.

This thesis contributes to the literature by evaluating how a lightweight deep learning detector (YOLOv5n) performs across different orbital configurations, focusing on the interplay between inference performance and orbital energy conditions. Unlike prior work that centers on algorithm benchmarking, this study emphasizes the mission-level trade-offs involved in deploying AI-based detection pipelines on real or simulated satellite platforms.

2.7.4 Energy-Aware Mission Design for Onboard AI

While the feasibility of onboard AI is well-established, energy consumption remains a primary constraint for mid-size satellites [21]. The design and management of satellite power systems is a mature field, with established methodologies for creating power budgets for various subsystems [36]. However, most of this work focuses on traditional payloads with predictable power draws.

The integration of high-performance edge processors for AI tasks introduces a new layer of complexity. The power consumption of these systems is not constant; it is highly dynamic and directly tied to the execution of specific tasks like AI inference. Recent studies have begun empirically measuring the energy consumption of ML models on edge hardware, confirming that model architecture and hardware choice are key drivers of the power budget [37]. Despite this progress, there remains a significant gap in connecting these hardware-level energy benchmarks to high-level mission design choices, such as orbital parameters.

Summary and Contribution of this Thesis

Prior research has established the benefits of SSO for consistent illumination, the potential of NSSO for flexible revisits, the feasibility of onboard edge AI, and the effectiveness of YOLO-based models for aircraft detection.

However, these areas have been largely investigated in isolation. Few studies have explicitly quantified how the choice of orbital parameters (inclination, RAAN, etc.) directly impacts the energy efficiency of an onboard AI surveillance mission. While many papers benchmark the accuracy of models like YOLOv5, they do not typically analyze how the model's operational requirements, such as the need for daylight visibility and sufficient image resolution (GSD), interact with orbital mechanics and the satellite's power budget.

This thesis addresses this critical gap. It moves beyond separate analyses of orbit design and AI performance by creating an integrated framework. The primary contribution of this work is the quantitative evaluation of the trade-off between visibility opportunities and energy consumption, directly linking orbital parameters to the operational efficiency of a realistic, AI-powered surveillance mission. In doing so, it provides a mission-level perspective on the deployment of power-intensive AI systems on energy-constrained satellite platforms.

Building on the insights and limitations outlined in this chapter, the following section presents the methodological framework of this study. It details the assumed system architecture, orbital simulation setup, object detection model, and key parameters used to evaluate the trade-offs between orbital configurations, daylight visibility, and onboard AI performance.

Chapter 3

METHODOLOGY

In this chapter, we outline the methodology used to analyze the trade-offs between target visibility and energy efficiency in SSOs and NSSOs for a LEO satellite tasked with airplane detection. The chapter presents a specific approach, including the simulation tools, key operational parameters, and core assumptions that underpin comparative analysis.

3.1 *Overview of Experimental Approach*

This study evaluates the performance of various LEO configurations for airplane detection over a fixed ground target, using edge computing onboard. The core methodology consists of the following key components:

- **Orbit simulation** of multiple SSO and NSSO configurations, implemented via custom Python scripts and validated using the General Mission Analysis Tool (GMAT).

- **Visibility analysis** over the target region (Incheon Airport), involving the extraction of key pass characteristics and the application of a composite scoring framework to rank orbit performance.

- **Definition of the onboard system**, including specifications for the imaging payload, edge processing hardware (NVIDIA Jetson Xavier NX), and the AI model (YOLOv5n) used for object detection.

- **Energy consumption modeling** to estimate the power required during active mission phases involving data acquisition and inference.

- **Efficiency evaluation** comparing orbital configurations based on the trade-off between visibility-driven detection opportunities and energy expenditure.

The subsequent sections of this chapter elaborate on each component of this experimental pipeline.

3.2 *Orbit Simulation and Visibility Evaluation*

This section details the methodology employed to simulate various LEO satellite configurations and evaluate their visibility over Incheon International Airport (ICN). First, it describes the orbital simulation setup using a Python-based analytical propagator, incorporating the J2 perturbation model, fixed mission parameters (such as orbital altitude and epoch), and the simulation timeframe and step size. Next, it specifies the range of orbital elements explored for SSOs and NSSOs—including Mean Anomaly, inclination, Right Ascension of the Ascending Node (RAAN), and Argument of Perigee (AOP)—along with the visibility criteria (minimum elevation angle of 20° above ICN) used to define valid observation opportunities and the key output metrics recorded (maximum single pass duration, total visible duration, and number of passes). Finally, it presents the methodology for quantitatively comparing the visibility performance of different orbital configurations, detailing the normalization of visibility metrics and the formulation of weighted composite scores for 1-day and 7-day analysis periods, along with the rationale behind the chosen weights.

3.2.1 Simulation Setup and Configuration

The orbital simulations in this study were implemented primarily using custom Python scripts employing analytical propagation methods. These methods specifically accounted for Earth's oblateness perturbation (J_2) to predict the secular evolution of the orbital elements. At each simulation timestep, the Right Ascension of the Ascending Node (RAAN, Ω), Argument of Perigee (AOP, ω), and Mean Anomaly (M) were updated from their initial values (Ω_0, ω_0, M_0) using the following J2-perturbed secular rates:

$$\Omega(t) = \Omega_0 + \dot{\Omega}_{J2} \cdot t \tag{3.1}$$

$$\omega(t) = \omega_0 + \dot{\omega}_{J2} \cdot t \tag{3.2}$$

$$M(t) = M_0 + \dot{M}_{J2} \cdot t \tag{3.3}$$

The detailed formulations for the secular rates of RAAN ($\dot{\Omega}_{J2}$) and AOP ($\dot{\omega}_{J2}$) were previously defined in Chapter 2 (Equations 2.1 and 2.2). The secular rate for the mean anomaly ($\dot{M}_{J2}$)

incorporates adjustments to the unperturbed mean motion (n) to account for J2 effects, calculated as:

$$\dot{M}_{J2} = n + \frac{3}{4} J_2 \left(\frac{R_E^2}{p^2} \right) n(3\cos^2(i) - 1) \tag{3.4}$$

In these equations, t represents the simulation time elapsed from the initial epoch. The term n denotes the unperturbed mean motion, calculated as $n = \sqrt{\mu/a^3}$, where μ is Earth's standard gravitational parameter and a is the semi-major axis. The parameter p is the semi-latus rectum of the orbit, given by $p = a(1 - e^2)$, where e is the orbital eccentricity. Other parameters (J_2, R_E, i) follow the standard definitions from Section 2.1. All initial conditions were set consistently at the simulation epoch of 20 March 2025, 00:00 UTC.

The overall computational flow for propagating the satellite's state and determining its geodetic position at each timestep involved the following sequence:

1. Initialize classical orbital elements: $a, e, i, \Omega_0, \omega_0, M_0$.

2. Compute the unperturbed mean motion n and the semi-latus rectum p.

3. Calculate the secular rates perturbed by J2: $\dot{\Omega}_{J2}, \dot{\omega}_{J2}, \dot{M}_{J2}$ using Equations 2.1, 2.2, and 3.4.

4. Propagate RAAN, AOP, and Mean Anomaly to the current time t using Equations 3.1-3.3.

5. With the updated Mean Anomaly $M(t)$ and eccentricity e, solve Kepler's equation to find the true anomaly (or eccentric anomaly first).

6. Using the true anomaly and other updated elements, transform from the perifocal coordinate frame to the Earth-Centered Inertial (ECI) frame to obtain the satellite's Cartesian position.

7. Convert the ECI position to geodetic coordinates (latitude, longitude, altitude above ellipsoid).

8. Store the resulting latitude and longitude for subsequent line-of-sight visibility analysis with respect to Incheon International Airport (ICN).

As one of the world's busiest international airports located at a strategic mid-latitude, ICN serves as a representative and challenging target for a responsive aerial surveillance mission. The airport is located at a latitude of 37.4602° N and a longitude of 126.4407° E [38].

All simulations were conducted at a nominal altitude of 685 km, consistent with the mission parameters of the KOMPSAT-3 satellite [27]. The simulations spanned both 1-day (86,400 seconds) and 7-day (604,800 seconds) durations, using a time step resolution of 1 second. The orbital trajectories and visibility calculations obtained from these Python-based simulations were cross-validated using NASA's General Mission Analysis Tool (GMAT) to ensure their reliability.

3.2.2 Parameter Sweep and Visibility Criteria

For the baseline SSO configuration, the inclination was selected to be consistent with the operational parameters of the KOMPSAT-3 satellite, which serves as the baseline for the assumed optical sensor characteristics in this study; this resulted in a fixed inclination of approximately 98.12° [27]. This chosen inclination, in conjunction with the 685 km altitude and near-circular eccentricity ($e = 0.0001$), also satisfies the requirements for a sun-synchronous condition, as it provides the necessary nodal precession rate calculated using standard orbital mechanics formulations (detailed in Section 2.2.1). Given the near-circular nature of the orbit, variations in the Argument of Perigee (AOP) have a negligible impact on ground track and illumination conditions for this SSO case and were therefore not varied as an independent parameter.

Since the simulation epoch for all analyses was fixed (March 20, 2025, 00:00 UTC), the Mean Anomaly (M0) defines the satellite's initial position along its orbital path at this specific epoch time. Since this starting position directly influences the timing and geometry of subsequent passes over the target (Incheon Airport), and consequently affects the raw visibility metrics, a dedicated sweep across M0 from 0° to 350° (in 60° increments) was conducted. This sweep was essential to determine the optimal initial phasing of the satellite relative to the target for the fixed epoch. For each M0 value tested, the raw visibility metrics (maximum single pass duration, total visible duration, and number of passes, as defined in Section 2.3) were calculated. These metrics were then normalized and used to compute the 1-day and 7-day composite visibility scores (with its formulation detailed in Section 3.3 below). The M0 yielding the highest 1-day and 7-day composite scores was selected

as the optimal M0 for the baseline SSO, and its associated visibility metrics were recorded.

The NSSO configurations explored a broader parameter space. Inclinations ranged from low-mid latitude prograde orbits (45° to 85° in 5° increments), through polar orbits (90°), to high-inclination retrograde orbits (93° to 110° in 2°/1° increments).

Inclinations below 45° were intentionally excluded from the sweep, as preliminary GMAT simulations confirmed that such low-inclination orbits rarely passed over the Korean Peninsula. For example, a 33° orbit showed negligible intersection with the Incheon (ICN) target area. These orbits, while potentially offering favorable revisit rates at lower latitudes, were deemed unsuitable for the mission's mid-latitude surveillance focus.

For each combination of inclination, Right Ascension of the Ascending Node (RAAN; varied from 0° to 360° in 60° increments), and fixed Argument of Perigee (AOP = 0°), the NSSO simulation evaluated a discrete set of Mean Anomaly (M0) values (from 0° to 360°, in 60° steps). This systematic sweep was conducted to assess how initial orbital conditions influence the 1-day and 7-day visibility scores, and to ensure consistency with GMAT-based validation.

Although the orbital eccentricity was kept low in all cases ($e = 0.0001$ for SSO and $e = 0.001$ for NSSO), the inclusion of M0 variations—even in near-circular orbits—allowed the capture of subtle differences in access geometry. AOP was held fixed at 0°, as its impact is negligible under such low eccentricities.

A minimum elevation threshold of 20° was adopted to define valid observation opportunities. This value represents a standard operational compromise between maximizing signal quality and maximizing access time. Lower elevation angles ($< 10^\circ$) suffer from significantly increased atmospheric path length and are more susceptible to line-of-sight blockages, while a higher threshold ($> 30^\circ$) would severely reduce the duration of each valid pass. Therefore, a 20° threshold is a commonly used baseline in LEO satellite operations that ensures both reliable link quality and a reasonably long observation window for each pass. This off-nadir viewing requirement is well within the capabilities of the assumed KOMPSAT-3 class platform, which supports roll tilting of up to $+56^\circ$ and pitch tilting of up to $+30^\circ$ [27].

This flexibility is particularly advantageous for missions requiring increased observation frequency or specific timing constraints. In the context of this study, where the target site (ICN) lacks significant topographic obstructions, imagery acquired at 20° elevation remains viable. Additionally,

the AI-based object detection framework employed is robust to moderate spatial distortion and resolution degradation, making this trade-off between image quality and access opportunity acceptable for the mission objectives.

3.3 *Visibility Scoring Methodology*

To quantitatively compare the performance of hundreds of different orbital configurations, this study employed a weighted composite scoring framework. This framework enabled a global ranking of candidate orbits based on key daytime visibility metrics: maximum single pass duration, total visible duration, and number of passes.

3.3.1 Raw Metric Evaluation and Composite Score

Each orbit configuration - defined by its unique combination of inclination, RAAN, AOP, and M0 - was propagated for a fixed simulation duration (either 1 or 7 days). For each configuration, raw visibility metrics were calculated based on daylight-only access windows at Incheon International Airport.

Before aggregation, each metric was normalized using Min-Max scaling (using `MinMaxScaler` from *sklearn.preprocessing*) across the full dataset. This ensures that metrics with different units or numerical ranges contribute equitably to the final score.

3.3.2 Global Ranking and Orbit Selection

After normalization, the composite score was calculated as a weighted sum of the three metrics. Separate weightings were applied for 1-day and 7-day analyses to reflect different mission priorities. Once the scores were computed, all configurations were ranked globally, and the highest-performing orbits were selected for further analysis.

3.3.3 Composite Score Formulas

The composite scores were calculated using different weighting schemes for the short-term and long-term analyses to reflect shifting mission priorities.

The **1-day** composite visibility score (`composite_score_1day`) was calculated as a weighted sum of the normalized metrics:

$$\begin{aligned} \text{Score}_{\text{1Day}} = &(0.4 \times \text{Norm}(\texttt{max\_pass\_duration})) \\ &+ (0.4 \times \text{Norm}(\texttt{total\_visible\_duration})) \\ &+ (0.2 \times \text{Norm}(\texttt{num\_passes})) \end{aligned} \tag{3.5}$$

where $\text{Norm}(\cdot)$ represents the Min-Max normalized value of the metric.

The weights for the 1-day analysis were chosen to reflect the priorities for efficient airplane detection opportunities over the ICN target within a **24-hour timeframe**. Specifically:

- **Maximum Single Pass Duration(weight = 0.4, high):** This reflects the importance of having a long, continuous observation window during a single flyover, which potentially allows for higher quality observations due to favorable viewing geometry.

- **Total Visible Duration (weight = 0.4, high):** This emphasizes the significance of the cumulative access time provided by the orbit throughout the day.

- **Number of Passes (weight = 0.2, low):** This decision acknowledges that while revisit frequency is relevant, preliminary analysis suggested it might be less discriminative than duration metrics for comparing orbits over this specific short-term evaluation period.

This weighting scheme facilitates a balanced ranking of orbits based on these prioritized 1-day visibility characteristics.

For the **7-day analysis**, designed to assess sustained performance characteristics, a different weighting scheme is proposed for the composite score (`composite_score_7day`):

$$\begin{aligned} \text{Score}_{\text{7Day}} = &(0.3 \times \text{Norm}(\texttt{max\_pass\_duration})) \\ &+ (0.3 \times \text{Norm}(\texttt{total\_visible\_duration})) \\ &+ (0.4 \times \text{Norm}(\texttt{num\_passes})) \end{aligned} \tag{3.6}$$

In this longer-term evaluation, the relative importance shifts compared to the 1-day analysis. The rationale for the 7-day weights is as follows:

- **Maximum Single Pass Duration (weight = 0.3, moderate):** Although still important for observation quality, the emphasis on the single longest pass(`max_pass_duration`) is slightly reduced compared to the 1-day scenario.

- **Total Visible Duration (weight = 0.3, moderate):** Similarly, the cumulative access time, represented by the `total_visible_duration` metric, remains significant but receives slightly less weight than in the 1-day score.

- **Number of Passes (weight = 0.4, higher):** The frequency of observation opportunities gains importance for consistent monitoring over a full week. Regular revisits are crucial for capturing potentially transient events, such as the presence of an airplane, over an extended period. Therefore, this metric (`num_passes`) receives the highest weight in the 7-day score calculation.

The results section will detail the application of this 7-day score.

3.4 *Onboard Detection System Configuration*

3.4.1 System Workflow Overview

This section outlines the operational workflow of the onboard airplane detection system from data acquisition to result transmission. This sequence defines the active payload cycle that forms the basis for the energy consumption model detailed later in this Section 3.5. To conserve power, the workflow is triggered only during valid observation opportunities and consists of the following steps:

1. **Activation on Valid Pass:** The payload system remains in a low-power standby mode until the satellite begins a valid ”daytime pass” over the target, Incheon International Airport (ICN) [38]. A pass is considered valid when the satellite's elevation is above the defined minimum threshold 20° and the sun is above the local horizon at ICN.

2. **Image Capture:** Once activated, the satellite's Attitude Determination and Control System(ADCS) orients the optical payload towards the target area [39]. The sensor, with characteristics based on the KOMPSAT-3 AEISS [27], then captures a high-resolution image strip covering the airport.

3. **Onboard Processing (Edge AI):** Instead of immediately downlinking the large raw image file, the data are processed directly onboard using the NVIDIA Jetson Xavier NX edge computing hardware [35]. This approach significantly reduces data volume and latency, which is a primary motivation for employing edge computing in satellite missions [4]. The processing sequence involves:

   (a) **Tiling:** The large, captured image strip is divided into smaller, overlapping image patches (tiles) suitable for input into the fixed-size AI model [40].

   (b) **Inference:** The YOLOv5n model, optimized with TensorRT, performs inference on each tile to detect airplanes and generate bounding boxes with confidence scores [26, 32].

4. **Result Aggregation and Transmission:** The detection results from all tiles, such as the coordinates of detected airplanes, are aggregated into a single, small data packet. While the operational KOMPSAT-3 satellite utilizes a high-bandwidth X-band downlink for raw imagery, this mission's edge computing architecture makes such a link unnecessary [28]. Because only a compact data packet is downlinked, a standard S-band communication link is assumed for transmission to a ground station. This approach minimizes the use of a high-bandwidth downlink, which reduces data transmission latency and saves considerable time and energy [4].

Following completion of the transmission, the payload system returns to its low-power standby mode until the next valid pass. The specific sequence for this entire operational workflow is detailed in the flowchart in Figure 3.1. This approach, which allows for responsive and energy-efficient surveillance, is also visually contrasted with traditional satellite operations in Figure 2.5

3.4.2 Imaging Payload Assumptions

For the purposes of this study, the optical sensor is modeled after the Advanced Earth Imaging Sensor System (AEISS) on the KOMPSAT-3 satellite [27, 28]. This choice provides a realistic baseline for performance and power consumption. The key assumed specifications are:

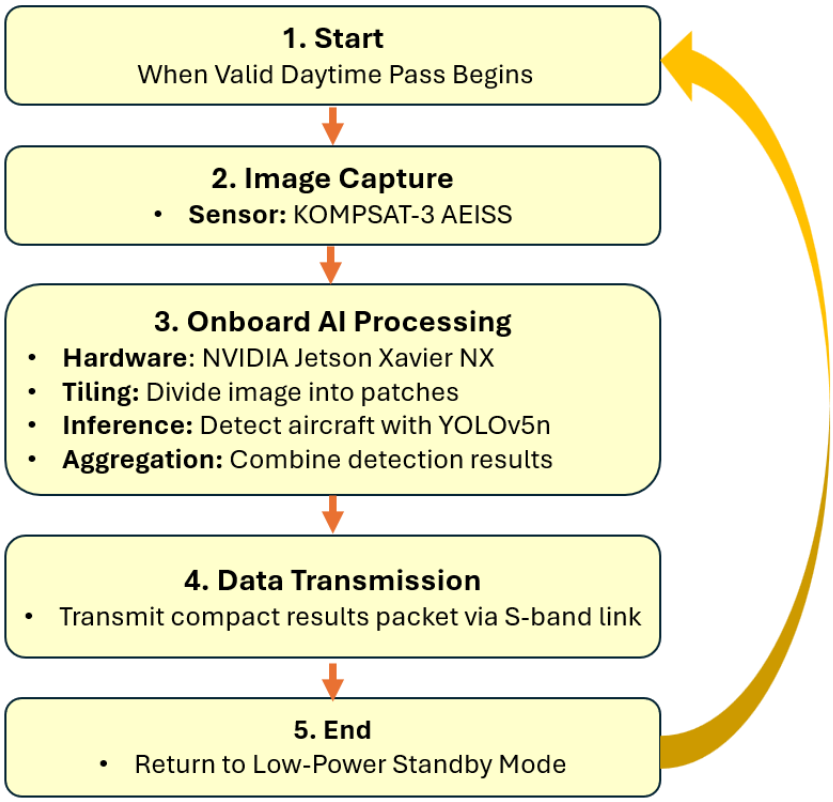

Figure 3.1: Flowchart of the simulated onboard system workflow for autonomous airplane detection

- **Resolution:** The KOMPSAT-3 AEISS sensor provides high-resolution panchromatic imagery with a GSD of approximately 0.7 meters at nadir [27, 33, 28]. For this study, we adopt a minimum target elevation angle of 20°, which results in a degraded resolution due to the increased slant range. As established in Section 2.3, the GSD for off-nadir observations scales approximately with the ratio of the slant range to the orbital altitude.

  To estimate the slant range R, we consider the satellite altitude $H \approx 685\,\text{km}$ and an elevation angle of 20°. Using the geometric relationship detailed previously in Section 2.3 (Figure 2.4), this yields a slant range of approximately $2000\,\text{km}$. Consequently, the effective off-nadir GSD becomes:

$$\text{GSD}_{\text{off-nadir}} \approx \text{GSD}_{\text{nadir}} \times \frac{R}{H} \approx 0.7\,\text{m} \times \frac{2000}{685} \approx 2.04\,\text{m} \tag{3.7}$$

This approximation is consistently used throughout this study, and the resulting 2.0-meter resolution is considered sufficient for reliable airplane detection with compact deep learning models such as YOLOv5n [7].

- **Swath Width:** The sensor is assumed to capture an image strip wide enough to cover the entirety of Incheon International Airport (ICN) in a single pass.

- **Agility:** The satellite is equipped with an Attitude Determination and Control System (ADCS) capable of pointing the sensor with precision towards the target area during a pass [39]. This study assumes that pointing is successfully achieved prior to image capture.

3.4.3 Edge Processing Hardware Assumptions

The onboard processing hardware is a critical determinant of system capability and efficiency. The following assumptions underpin the selection and operational considerations of the edge computing platform:

- **Hardware Platform:** The NVIDIA Jetson Xavier NX is chosen as the onboard edge computing hardware due to its strong balance between computational performance and energy efficiency, making it particularly suitable for resource-constrained mid-size satellite platforms. Its compact form factor, relatively low-power consumption (typically between 10 and 20 watts), and robust GPU capabilities (up to 21 TOPS—Tera Operations Per Second) [25] align well with the Size, Weight, and Power (SWaP) constraints inherent to LEO missions [5, 35, 21]. Detailed selection rationale and hardware characteristics are discussed previously in Section 2.4.

- **Software Environment:** The onboard inference utilizes NVIDIA's CUDA framework and TensorRT optimization library. Specifically, the YOLOv5n model deployed onboard is assumed to be optimized through TensorRT, significantly reducing inference latency and energy consumption compared to standard implementations [26]. Such optimizations are essential

for achieving the rapid inference speeds required for time-constrained, energy-aware satellite operations [5, 11].

Although conducted in a terrestrial context, benchmark experiments by Tang et al. [41] deploying YOLOv5 models on the Jetson Xavier NX platform showed that TensorRT optimization increased inference speed from 17 FPS to 33 FPS, corresponding to a 2 times reduction in latency. Based on these results and similar edge AI deployments, this study assumes a comparable performance improvement in the satellite's onboard setting.

- **Inference Load per Pass:** For each satellite pass over ICN, the captured imagery is segmented into approximately 20–40 tiles, each sized 640×640 pixels, suitable for input to the YOLOv5n model. This inference load directly influences the minimum required inference speed.

- **Performance (Frames Per Second - FPS):** Accurately estimating onboard inference throughput is essential to ensure that the satellite can process all acquired imagery within the short windows of visibility. Based on benchmark results from Tang et al. [41], the NVIDIA Jetson Xavier NX achieves approximately 33 frames per second (FPS) when running a TensorRT-optimized YOLOv5 model. This corresponds to a per-tile processing time of about 0.03 seconds, which is used as the baseline for this study's energy and performance modeling.

  Given the number of image tiles generated per image strip and the typical pass durations observed in simulation—ranging from approximately 100 to 400 seconds—this processing throughput provides sufficient margin to complete onboard inference within each pass window. It ensures that all captured data can be processed in real time, aligning with the constraints of energy-aware task execution in LEO satellite operations.

- **Inference Energy Consumption and Duration:** According to the hardware's official specifications and typical power modes [25], each inference cycle per image tile on the Jetson Xavier NX is assumed to consume around 10–20 watts of power. This power draw, combined with the high-speed performance, results in an inference duration of approximately 30 milliseconds per tile [41]. These benchmarks provide the foundational data for the detailed energy consumption modeling presented later in Section 3.5.

- **Thermal and Radiation Assumptions:** Explicit thermal management and radiation shielding strategies were not modeled in this study. It was assumed that the hypothetical satellite platform design adequately manages these environmental factors to maintain nominal operational conditions for the Jetson Xavier NX hardware.

These operational assumptions define realistic boundary conditions, enabling robust satellite mission simulation and accurate energy modeling analyses.

3.4.4 Object Detection Model (YOLOv5n)

For the onboard airplane detection task in this study, the You Only Look Once version 5 nano (YOLOv5n) model was selected. This decision was influenced by recent comprehensive comparative reviews, such as El Ghazouali et al. (2024), which identified YOLOv5 as a pre-eminent model for identifying airplanes from remote sensing data due to its high precision and adaptability across diverse imaging conditions [7]. Our selection of the 'nano' variant (YOLOv5n) further prioritizes computational efficiency, crucial for resource-constrained satellite edge computing platforms, while aiming to retain acceptable detection accuracy.

To confirm its suitability and characterize its performance in relation to the larger variants for this study, initial comparative experiments with YOLOv5s and YOLOv5m were performed. Model training and these initial evaluations were performed using a T4 GPU accessed via the Google Colab environment. The characteristics and 10-epoch training performance are summarized in Table 3.1. YOLOv5n demonstrated a significantly reduced computational footprint, with only 214 layers, approximately 1.77 million parameters, and 4.2 GFLOPS required for inference. Table 3.1 summarizes the key structural and performance characteristics of YOLOv5n compared to the larger variants YOLOv5s and YOLOv5m.

Despite its compact size, the selected YOLOv5n model achieved robust detection performance, with a precision consistently above 0.95, making it well-suited for the application in this study. To explore performance improvements with extended training, the model was trained for 20 epochs, after which it reached a precision of 0.968, recall of 0.960, mean Average Precision at an IoU threshold of 0.50 (mAP@0.50) of 0.983, and a mAP@0.50–0.95 of 0.717. Testing on a dedicated hold-out set further corroborated its performance, yielding mAP@0.50 of 0.976 and mAP@0.50–0.95 of 0.634.

Table 3.1: Comparison of YOLOv5 Model Variants (10 Epochs on Google Colab T4 GPU)

Feature	YOLOv5n	YOLOv5s	YOLOv5m
Layers	214	214	291
Parameters (Millions)	1.77	7.02	20.87
GFLOPS	4.2	15.9	48.2
Precision (P)	0.961	0.969	0.977
Recall (R)	0.973	0.969	0.977
mAP@0.50	0.936	0.985	0.990
mAP@0.50-0.95	0.651	0.715	0.765
Training Time (Hours)	0.556	2.517	2.596

These metrics affirm YOLOv5n's effectiveness for the specific task of airplane detection, aligning with findings by El Ghazouali et al. (2024), who reported strong AP, recall, and IoU performance for YOLOv5-based aircraft detection models [7] (where IoU, or Intersection over Union, measures the overlap between predicted and ground truth bounding boxes).

The model was trained and validated using the HRPlanesv2 dataset, which consists of 2,120 very high-resolution (VHR) Google Earth images of global airports, encompassing a total of 14,335 labeled aircraft instances. Each image, with a resolution of 4800×2703 pixels, is accompanied by annotation files in the YOLO `.txt` format. The dataset was partitioned into 70% for training, 20% for validation, and 10% for testing [29].

To evaluate robustness under various imaging conditions, an additional test set of 198 synthetically modified images was used. These included variations in brightness, clarity, and coloration to simulate environmental conditions such as sunrise, sunset, and atmospheric haze. In this set, YOLOv5n retained a high classification accuracy (mAP @ 0.50 of 0.995), although the precision of the bounding box decreased, with mAP @ 0.50-0.95 reduced to 0.515. This drop illustrates the sensitivity of spatial localization to environmental variability and underscores the importance of stable imaging conditions or adaptive retraining for consistent performance in operational scenarios.

3.4.5 Data Transmission Assumptions

Following onboard processing, only the results are transmitted to the ground.

- **Data Volume:** The transmitted data is not raw imagery but a small packet containing detection results such as locations of airplanes, counts, and confidence scores. This reduces the data volume by several orders of magnitude compared to the raw image file [4, 11].

- **Communication Link:** A standard S-band transmitter is assumed for the downlink. This is a common choice for satellite telemetry and low-volume data transmission and has a correspondingly moderate power requirement [42].

3.5 *Energy Performance Model*

To evaluate the trade-off between visibility and power, a comprehensive performance model was developed. It measures both the electrical load from the payload and the solar energy harvested by the satellite, as estimated through a simplified geometric model developed for this study. In this section, we assess the power demands of all previously introduced operations, including image capture, onboard inference, and data transmission under realistic orbital conditions [43, 25, 44]. By comparing total consumption against generation, we compute a net energy balance that serves as a clear indicator of long-term orbital sustainability.

3.5.1 Energy Consumption Model

The energy consumption model focuses on the use of the payload's electrical power, as this is the variable component directly influenced by the number and duration of observation opportunities. The model calculates consumption on the basis of two distinct operational states: a high-power "active cycle" during useful observations and a low-power "standby mode" for all other times [44].

Active Payload Cycle

The payload is considered "active" only during a **daytime pass**, which is a period that meets two criteria simultaneously: (1) the satellite has geometric visibility of the target (elevation $> 20^{\circ}$) [7], and (2) the target is illuminated by the sun.

Multiple image strips are acquired during extended visibility windows, rather than assuming only a single imaging event per pass [27, 33].The total number of strips, N_{strips}, is determined by the duration of the pass and a fixed imaging interval of $\Delta t_{\text{interval}} = 2.0$, seconds. This value represents a conservative power-sensitive operational mode, rather than the maximum 2 Hz (0.5-second interval) capture rate of agile satellites such as LuoJia3-01 [45]. The number of strips is computed as follows:

$$N_{\text{strips}} = \left\lfloor \frac{\text{Pass Duration}}{\Delta t_{\text{interval}}} \right\rfloor \tag{3.8}$$

The total energy consumed during the pass, E_{pass}, is the product of the number of strips and the energy of a single active strip cycle, $E_{\text{active\_strip}}$:

$$E_{\text{pass}} = N_{\text{strips}} \times E_{\text{active\_strip}} \tag{3.9}$$

where $E_{\text{active\_strip}}$ is defined as:

$$E_{\text{active\_strip}} = E_{\text{capture}} + E_{\text{process}} + E_{\text{transmit}} \tag{3.10}$$

The components of this active cycle are based on a representative hardware suite for an advanced LEO surveillance mission:

$E_{\textbf{capture}}$**:** The energy for image acquisition is the product of the optical payload's peak power draw ($P_{\text{capture}} = 300.0\,\text{W}$) [43]and the capture duration ($t_{\text{capture}} = 0.1\,\text{s}$) [27]. This duration corresponds to a short imaging interval in which approximately 1100 image lines are captured by a pushbroom-style sensor, a figure derived from the sensor's specified line scan time. [27]. The power estimate is based on the L3Harris SpaceView-80 (SV-80) payload, a high-resolution imager with specifications closely matching those of KOMPSAT-3 [43].

$E_{\textbf{process}}$**:** The energy for onboard AI inference using the YOLOv5n object detection model. The total processing energy is the product of the power draw of the NVIDIA Jetson Xavier NX ($P_{\text{process}} = 15.0\,\text{W}$) and the cumulative inference time for all tiles within a captured image strip [25]. To process the captured image, the full strip is divided into smaller square tiles of size 640×640 pixels [26] with a 20% overlap [40]. For a typical image strip ($24{,}000 \times 1{,}100$ pixels), the total number of tiles [40, 27, 28], N_{tiles}, is computed as:

$$\text{step\_size} = \text{tile\_size} \times (1 - \text{overlap\_ratio}) \tag{3.11}$$

$$N_{\text{tiles,horiz}} = \left\lceil \frac{\text{pixels\_across\_swath} - \text{tile\_size}}{\text{step\_size}} \right\rceil + 1 \tag{3.12}$$

$$N_{\text{tiles,vert}} = \left\lceil \frac{\text{lines\_per\_strip} - \text{tile\_size}}{\text{step\_size}} \right\rceil + 1 \tag{3.13}$$

$$N_{\text{tiles}} = N_{\text{tiles,horiz}} \times N_{\text{tiles,vert}} \tag{3.14}$$

E_{transmit}: The energy for data downlink, accounting for transmitting a small result packet using a standard S-band transmitter ($P_{\text{transmit}} = 10.0\,\text{W}$) for a brief duration ($t_{\text{transmit}} = 0.01\,\text{s}$). This value reflects the upper-range transmit power supported by modern low-Earth orbit TT&C modules such as the SSTRX-1000, which offers configurable RF output up to 10 W [46].

Standby Power Consumption

During all periods when the payload is not in an active observation cycle, the satellite remains in a low-activity state. In this model, the standby power (P_{standby}) is set to $250.0\,\text{W}$ to reflect the **total average power consumption of the entire satellite bus**, including the Attitude Determination and Control System (ADCS), onboard computer (OBC), thermal control systems, and other essential subsystems, as well as the idle payload electronics [39]. This value represents approximately 19% of the 1.3 kW total onboard power capacity of KOMPSAT-3, a mid-size EO satellite [28]. It offers a more realistic estimate of total power requirements and a clearer view of long-term energy sustainability.

3.5.2 Energy Generation Model

To provide a realistic assessment of the energy available, a full-orbit energy generation model was implemented. This model calculates the power produced by the satellite's solar panels at every time step in the simulation, accounting for orbital position, satellite attitude, and the angle of the Sun based on standard solar geometry estimation [1].

Solar Panel Configuration: The model assumes a representative solar panel system with a total surface area of $\mathbf{3.8}\,\text{m}^2$ and a standard cell efficiency of $\mathbf{29.5}\%$, consistent with modern triple-junction GaAs solar arrays used on mid-size EO satellites [1, 28]. The total area is distributed across four panels mounted on the faces of the satellite body (+X, -X, +Y, -Y).

Satellite Attitude: A nadir-pointing attitude is assumed, where one axis of the satellite is always oriented towards the center of the Earth. This is a standard operational mode for Earth-observation missions [1, 39].

Power Calculation: At each time step, the simulation determines if the satellite is in direct sunlight or eclipsed by the Earth. If in sunlight, it calculates the vector to the Sun and the satellite's orientation. The angle between the Sun's rays and the normal vector of each solar panel is then computed. The power generated is proportional to the cosine of this angle, following standard solar panel modeling practices [39, 36]. The total energy generated is the integral of this power over the entire simulation duration.

3.6 *Efficiency Evaluation Metrics*

To provide a clear, quantitative basis for comparing the mission effectiveness of each orbital configuration, the following metrics are defined. These metrics are designed to directly evaluate the trade-off between useful observation opportunities and the required energy expenditure.

Total Strips Captured: This metric counts the total number of images acquired over the simulation period. It serves as a direct measure of an orbit's potential for providing raw data volume.

Net Energy Balance: This is the primary metric for assessing mission sustainability. It is calculated by subtracting the total energy consumed from the total energy generated over the entire simulation period. A positive value indicates an energy surplus, making the orbit sustainable, while a negative value indicates an energy deficit.

Strips per Kilojoule (kJ): This normalized metric is calculated by dividing the Total Strips Captured by the Total Energy Consumed (in kJ). It represents the average data return for each unit of energy spent and is a key indicator of mission efficiency. A higher value signifies a better return on energy investment.

Final Efficiency Score: The ultimate ranking is determined by a 'composite efficiency score', which combines a 'visibility score' and an 'energy score'. The visibility score is a weighted sum

of normalized values for total strips captured, maximum pass duration, and the number of daytime passes. The Energy Score is the normalized net energy balance. These two scores are then combined with equal weighting (50/50) to produce a final, holistic measure of an orbit's overall performance. The specific weights for the Visibility Score components are adjusted based on the simulation duration to reflect their relative importance:

- **For the 1-Day Simulation:** The weights are set to prioritize pass duration and data volume, with less emphasis on the raw number of passes. The weights are: max pass duration (0.3), total visibility duration (0.3), number of passes (0.1), and total strips (0.3).
- **For the 7-Day Simulation:** Over a longer period, the frequency and reliability of passes become more significant. Therefore, the weight for the number of passes is increased. The weights are: max pass duration (0.2), total visibility duration (0.2), number of passes (0.3), and total strips (0.3).

Chapter 4

RESULTS AND ANALYSIS

This chapter presents the quantitative results from the comparative analysis of the selected orbital configurations. The analysis follows the methodology from Chapter 3, identifying the best performing orbits from a global parameter sweep, evaluating their visibility characteristics, and quantifying mission efficiency through onboard energy modeling. The analysis spans both 1-day (short-term) and 7-day (long-term) simulation periods, providing a comprehensive assessment of how simulation duration and mission priorities influence the selection of optimal orbits.

4.1 1-*Day Simulation Analysis*

The short-term analysis focuses on maximizing immediate access and data acquisition opportunities within a single 24-hour window.

4.1.1 Selected Orbit Configurations for Analysis

To conduct a comprehensive performance comparison, a diverse set of six representative candidates were chosen based on the results of the global parameter sweeps. The selection includes a baseline SSO and five high-performing NSSOs.

NSSO candidates were chosen to test performance in a range of promising inclinations. An initial review of the global sweep data revealed that the highest-scoring orbits were heavily clustered around a 45° inclination. To validate this finding and explore the performance sensitivity, the candidate that performed the best in the 45° group was selected, along with the orbits that performed the best in the 50°, 60°, 70°, and 110° inclination classes. This approach ensures that the analysis compares fundamentally different orbital strategies, providing a clear insight into their respective trade-offs.

The final selected configurations for the analysis are summarized in Table 4.1.

Table 4.1: Selected orbit configurations for comparative analysis

Orbit Label	**Alt. (km)**	**Inc. (°)**	**RAAN (°)**	**AOP (°)**	**M0 (°)**
SSO-1d	685	98.12	300	0	0
NSSO-1d-45	685	45.00	60	0	300
NSSO-1d-50	685	50.00	60	0	300
NSSO-1d-60	685	60.00	120	0	180
NSSO-1d-70	685	70.00	120	0	180
NSSO-1d-110	685	110.00	240	0	60

4.1.2 Visibility Performance (1-Day)

The key visibility metrics for the selected orbits are summarized in Table 4.2.

Table 4.2: 1-Day Daytime Visibility Performance Comparison

Metric	**SSO-1d**	**NSSO-1d-45**	**NSSO-1d-50**	**NSSO-1d-60**	**NSSO-1d-70**	**NSSO-1d-110**
Max Single Pass Duration (s)	362	**400**	400	400	370	370
Total Daytime Duration (s)	661	**1960**	1500	990	1020	600
Number of Daytime Passes	2	**6**	6	4	3	2
visibility composite score	0.55	**0.99**	0.90	0.73	0.67	0.55

The results in Table 4.2 reveal a stark contrast in performance between the different orbit classes. The mid-inclination NSSO configurations demonstrate a clear superiority over both the high-inclination SSO and the retrograde NSSO-110 orbit.

The **NSSO-1d-45** orbit emerges as the top performer, delivering the longest total daytime duration (1960s) and the highest visibility score (0.99). Although the NSSO-1d-50 configuration provided one additional pass, the exceptional duration of the NSSO-1d-45 passes made it the most effective for maximizing data acquisition within the 24-hour window. A clear trend is also observable where performance generally decreases as the inclination increases from 45° towards 90°. This analy-

sis underscores the significant operational advantage of mid-inclination NSSOs for time-sensitive surveillance tasks that prioritize long, continuous observation periods.

4.1.3 Ground Track Comparison

To visually support the visibility performance analysis, Figure 4.1 compares the ground tracks of the baseline SSO-1d orbit and the most effective NSSO-1d-45 configuration. Each orbit is shown using both the custom Python-based propagator and GMAT for validation.

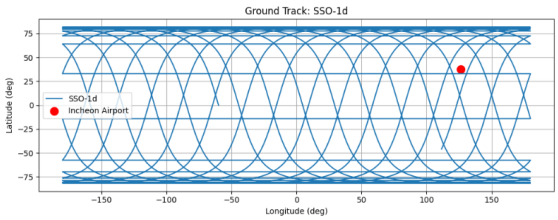

(a) SSO-1d (Python)

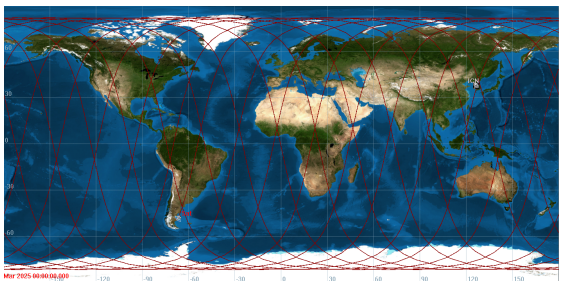

(b) SSO-1d (GMAT)

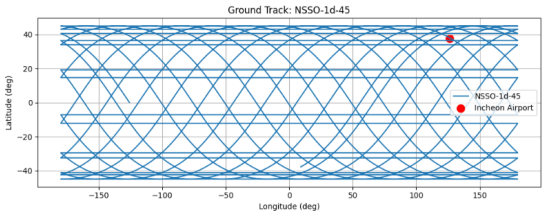

(c) NSSO-1d-45 (Python)

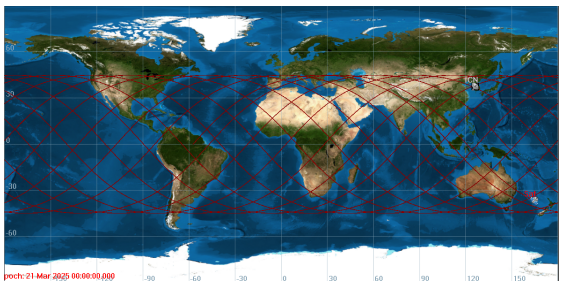

(d) NSSO-1d-45 (GMAT)

Figure 4.1: Ground tracks for SSO-1d and NSSO-1d-45 over a 24-hour period. Each orbit is shown using both Python propagation and GMAT for cross-validation.

These visualizations clearly demonstrate the spatial differences in coverage patterns. While the SSO maintains a global, pole-to-pole swath consistent with its sun-synchronous design, it only passes over the target region—Incheon Airport—twice during the 24-hour window. In contrast, the NSSO-1d-45 configuration, despite covering a narrower latitude band focused around the mid-latitudes,

exhibits a much denser clustering of ground tracks near the target. This results in significantly more frequent and longer visibility opportunities over the target, thereby explaining the superior visibility composite score observed in Table 4.2.

4.2 7-*Day Simulation Analysis*

To understand sustained performance and long-term access patterns, the analysis was extended to a 7-day period.

4.2.1 Selected Orbit Configurations (7-Day)

The orbit selection process for the 7-day scenario follows the same principle as the 1-day case: prioritizing diversity in orbital geometry over raw score maximization. While mid-inclination NSSOs around 45° once again dominated the global rankings, their performance advantage became less distinct over a longer observation window.

To enable a broader comparison, the top NSSO configuration at 45° inclination was retained, and four additional candidates were selected from the 50°, 60°, 70°, and 110° classes—each representing the highest-scoring orbit within its group. This selection ensures meaningful trade-off evaluation across fundamentally different orbital dynamics. The baseline SSO configuration was included for continuity, and the final set of selected orbits is summarized in Table 4.3.

Table 4.3: Top-ranked orbit configurations for 7-day visibility evaluation.

Orbit Label	**Alt. (km)**	**Inc.** (°)	**RAAN** (°)	**AOP** (°)	**M0** (°)
SSO-7d	685	98.12	300	0	120
NSSO-7d-45	685	45.00	120	0	240
NSSO-7d-50	685	50.00	120	0	0
NSSO-7d-60	685	60.00	120	0	240
NSSO-7d-70	685	70.00	120	0	240
NSSO-7d-110	685	110.00	240	0	0

4.2.2 Visibility Performance (7-Day)

Over the 7-day period, the advantages of the NSSO configurations become even more pronounced, as shown in Table 4.4. They provide a significantly higher number of total daytime passes, demonstrating a superior capability to maximize detection opportunities over a sustained period. This is particularly crucial for responsive surveillance missions that aim to capture transient or unscheduled events.

Table 4.4: 7-Day Daytime Visibility Performance Comparison

Metric	**SSO-7d**	**NSSO-7d-45**	**NSSO-7d-50**	**NSSO-7d-60**	**NSSO-7d-70**	**NSSO-7d-110**
Max Single Pass Duration (s)	380	**410**	400	400	390	370
Total Daytime Duration (s)	3030	**12540**	10030	6730	5200	3860
Number of Daytime Passes	10	**37**	35	22	29	15
visibility composite score	0.49	**1.00**	0.91	0.69	0.62	0.53

Among the selected configurations, the mid-inclination NSSO at 45° not only achieves the highest number of daytime passes (37) but also records the longest single-pass duration (410 seconds) and the highest total daytime visibility (12,540 seconds). Other NSSO configurations such as those at 50° and 60° inclinations also outperform the baseline SSO across all visibility metrics, albeit with slightly reduced scores.

In contrast, the SSO configuration, while offering consistent sun-synchronous coverage, exhibits only 10 daytime passes over 7 days, with a total duration of 3,030 seconds. Its composite visibility score of 0.49 reflects this limitation, ranking well below all NSSO counterparts. These findings reinforce the conclusion that NSSO orbits can offer substantial visibility advantages when temporal flexibility is allowed.

4.3 *Energy Efficiency Analysis*

While visibility metrics define the opportunity for data acquisition, energy efficiency determines the sustainability and practicality of exploiting those opportunities. This section evaluates the energy budget and operational performance of the top-performing orbits identified in the visibility analysis.

4.3.1 1-Day Performance Trade-off

Although mid-inclination NSSO configurations offer markedly higher visibility and image acquisition potential, these advantages often come at the cost of increased power consumption. This section analyzes the trade-off between energy expenditure and data yield to determine which orbits provide the most efficient operational return on energy.

(1) Energy Budget Overview

Figure 4.2 shows the total energy generated and consumed by each orbit over a 24-hour period. The SSO generated the most solar energy because of its regular exposure to sunlight and minimal payload activity. However, its lower number of passes and fewer imaging opportunities resulted in the lowest data yield among all orbits.

In contrast, the high-visibility NSSO candidates, particularly NSSO-1d-45 and NSSO-1d-50, consumed significantly more power due to their frequent imaging and onboard inference operations. Despite operating near the limit of their available energy budgets, they remained energy-positive over the simulation period.

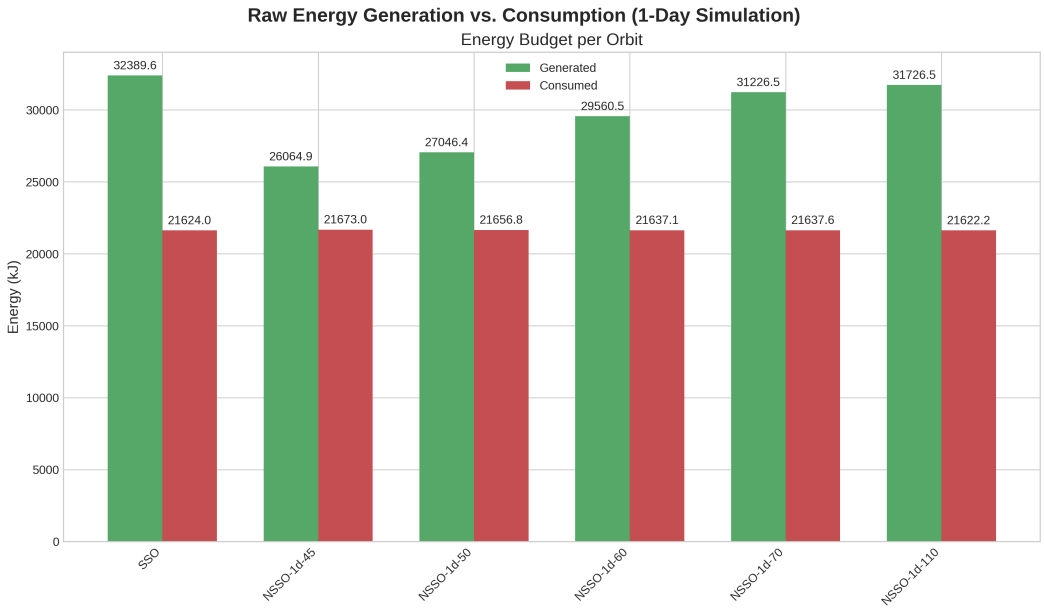

Figure 4.2: Raw energy generation vs. consumption for each orbit

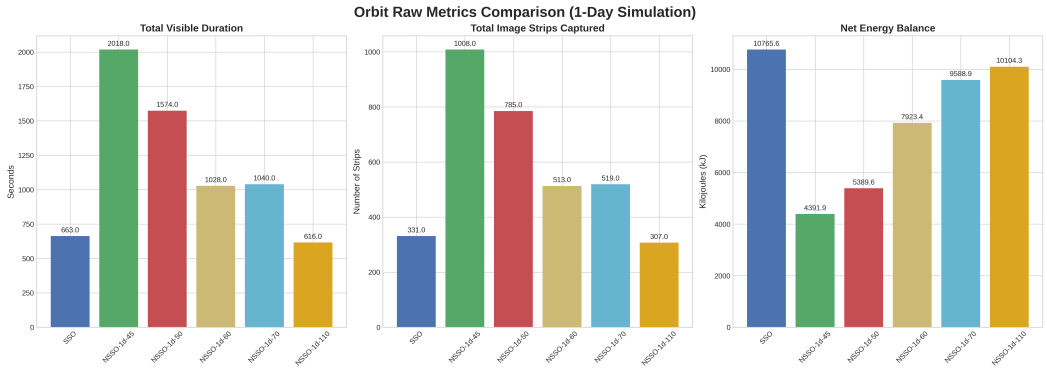

Figure 4.3: Raw 1-day metrics: (Left) total visible duration, (Centre) image strips captured, (Right) net energy balance.

Figure 4.3 complements the budget plot (Figure 4.2) by showing net energy balance alongside visibility-driven metrics. Placing it here clarifies how increased pass duration and strip count translate into higher energy expenditure.

(2) Data Efficiency Metrics

To enable a fair comparison across orbits with differing energy budgets, we evaluate how efficiently each configuration converts energy into actionable data. Figure 4.4 presents two derived metrics that

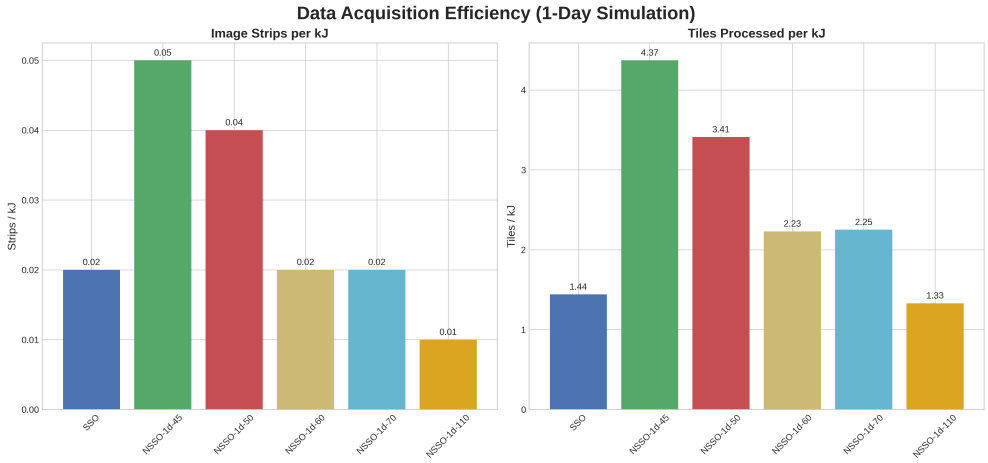

Figure 4.4: Data acquisition efficiency metrics (strips/kJ and tiles/kJ) for each orbit

normalize for energy consumption: **the number of image strips captured per kilojoule** and **the number of tiles processed per kilojoule**.

The first metric, strips/kJ, reflects how many full-width image swaths the satellite can acquire with a given amount of energy, indicating the efficiency of large-scale data acquisition. The second metric, tiles/kJ, goes one level deeper, measuring how many inference tiles—individual image patches processed by the AI model—are generated per unit of energy. This offers a finer-grained view of computational workload efficiency and more directly reflects how well the satellite supports onboard AI tasks.

Together, these two measures provide a more complete picture of operational efficiency: one captures how often the satellite collects data, while the other captures how intensively it processes that data onboard. A configuration that performs well on both axes is likely to be both data-rich and power-efficient.

The SSO showed the highest energy surplus (as shown in the previous section), yet delivered the lowest data yield per unit of energy. NSSO-1d-45 and NSSO-1d-50 captured the most data overall, but at a high energy cost per strip. While NSSO-1d-70 did not top the charts in either individual metric, it demonstrated consistently strong efficiency across both measures, indicating a well-balanced performance in terms of energy use and data acquisition.

Mission relevance: High tiles/kJ values are particularly valuable in edge AI missions, where onboard inference must be performed quickly and autonomously. By maximizing how much data is processed onboard per unit of energy, the system reduces downlink requirements and improves responsiveness—both of which are critical for time-sensitive tasks such as airplane detection.

(3) Final Efficiency Ranking

The final composite efficiency score—shown in Figure 4.5—integrates normalized visibility performance with energy sustainability. **NSSO-1d-70** secured the highest overall score (0.589), edging out NSSO-1d-45 and NSSO-1d-50. This confirms that the most effective orbit is not necessarily the one with the most data or the largest energy surplus, but the one that strikes the best balance between them.

This reinforces a central takeaway: while SSO offers strong energy headroom and NSSO-1d-45

excels at data collection, it is **NSSO-1d-70** that ultimately delivers the best "bang for the buck" in operational terms.

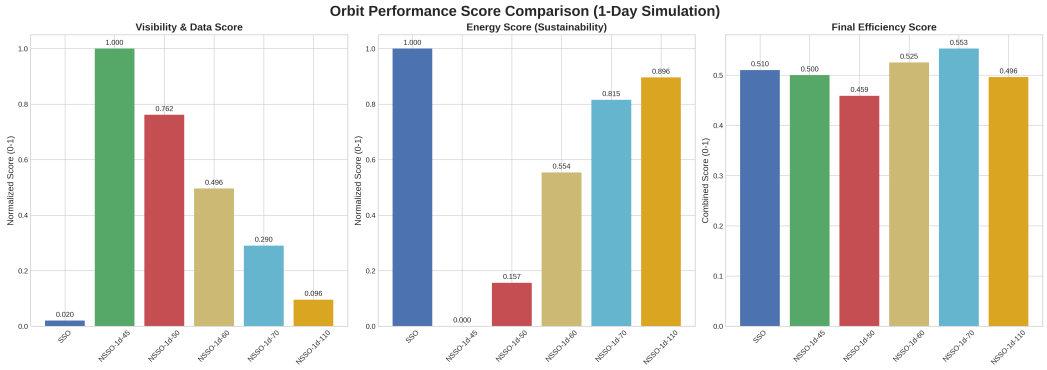

Figure 4.5: Composite visibility and energy-based efficiency scores for each orbit

4.3.2 Energy Efficiency Analysis (7-Day)

(1) Raw Energy Profile

Figure 4.6 compares the total energy generated and consumed by each orbit configuration over the 7-day simulation. Although the SSO and NSSO-7d-70 orbits produced the largest solar energy budgets, their energy usage patterns varied significantly. The SSO maintained the highest net energy surplus, reflecting its limited number of image acquisition opportunities and conservative power usage. In contrast, NSSO-7d-70 struck an ideal balance, sustaining high generation while efficiently utilizing energy for meaningful data collection.

Figure 4.7 provides the long-term counterpart, showing how NSSO-7d-45's prolific data yield is offset by a reduced energy margin, whereas NSSO-7d-70 maintains a healthier balance.

(2) Data Efficiency Metrics

To evaluate how well each orbit configuration converted available energy into actionable data, two normalized efficiency metrics were analyzed: the number of image strips captured per kilojoule (strips/kJ) and the number of tiles processed per kilojoule (tiles/kJ). The former reflects large-scale

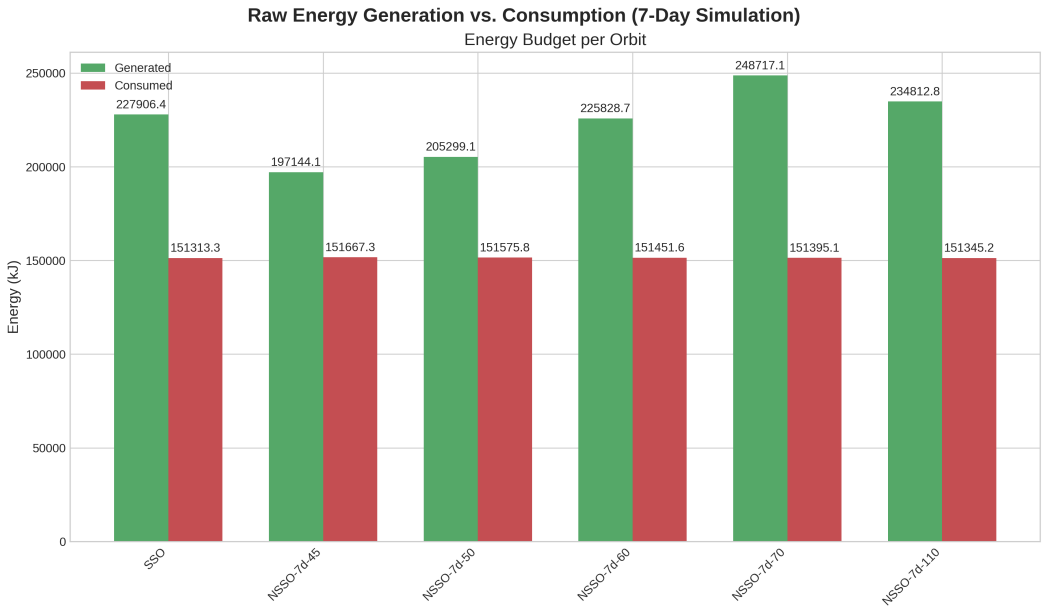

Figure 4.6: Total energy generation vs. consumption over 7 days for each orbit

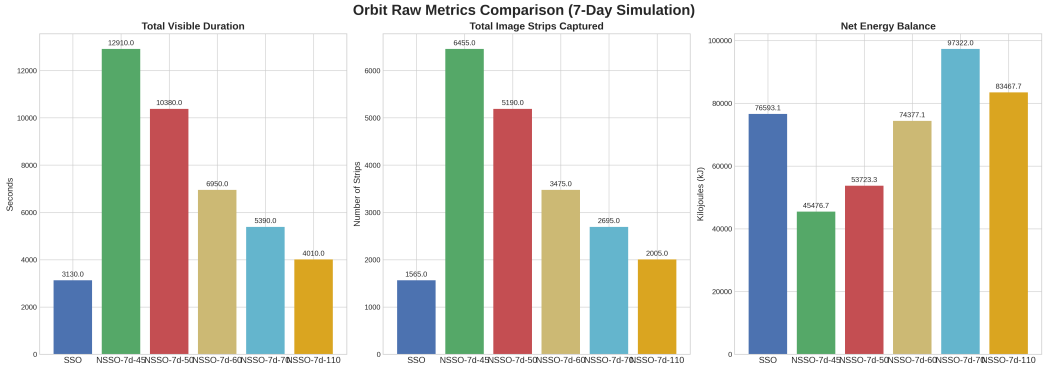

Figure 4.7: Raw 1-day metrics: (Left) total visible duration, (Centre) image strips captured, (Right) net energy balance.

acquisition efficiency, while the latter accounts for inference-relevant data volume, directly tied to onboard AI processing throughput.

As shown in Figure 4.8, NSSO-7d-45 outperformed all other configurations in both categories, capturing the most data per unit energy. This indicates that while its total energy budget was not the

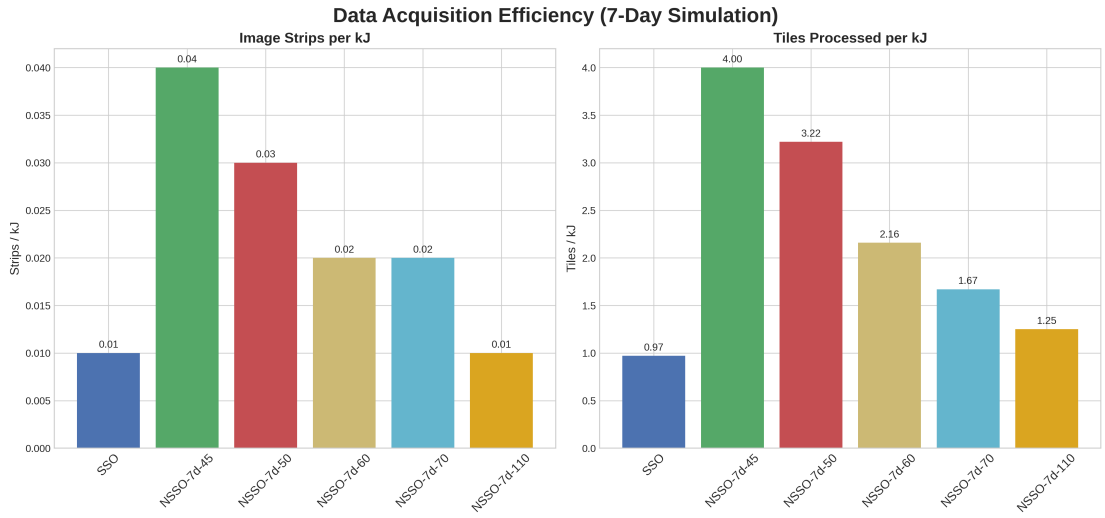

Figure 4.8: Normalized data efficiency metrics (strips/kJ and tiles/kJ) across orbits

highest, its operational use of energy was exceptionally productive from an edge AI perspective. On the other hand, SSO—despite its large energy surplus—demonstrated the lowest inference efficiency, again reinforcing that surplus alone is not indicative of effective mission yield.

(3) Final Efficiency Score

The final evaluation, shown in Figure 4.9, combines visibility performance and energy sustainability into a single composite score. NSSO-7d-70 emerged as the most balanced configuration, achieving the highest final efficiency score. It offered moderate data yield, strong energy balance, and acceptable inference efficiency—making it the most viable orbit when both mission yield and power constraints are considered.

Figure 4.9 presents the final composite efficiency scores for each orbit, integrating normalized visibility performance and energy sustainability. Among all configurations, **NSSO-7d-70** achieved the highest score, despite not leading in any single metric. This outcome underscores a key insight of the analysis: true operational efficiency does not stem from maximizing either visibility or energy alone, but from achieving a strong balance between the two.

Notably, **NSSO-7d-45** dominated visibility and data yield metrics, and **SSO-7d** maintained the highest energy surplus. Yet, both fell short in composite performance due to imbalanced trade-

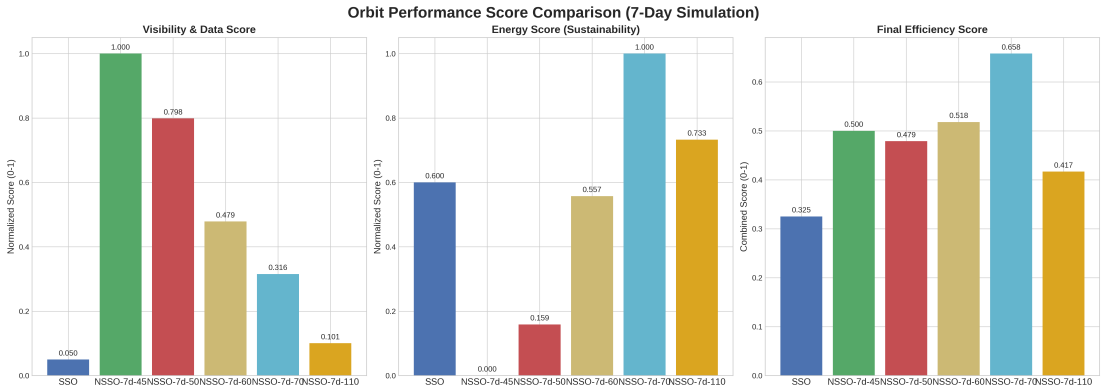

Figure 4.9: Final composite performance scores normalized across visibility and energy metrics

offs—either incurring high energy costs (NSSO-7d-45) or underutilizing available power (SSO-7d). By contrast, NSSO-7d-70 demonstrated consistent and moderate performance across visibility, energy use, and onboard inference efficiency, making it the most viable configuration from an end-to-end operational standpoint.

Mission relevance: For autonomous object detection tasks where both frequent access and energy constraints matter, orbits like NSSO-7d-70 represent a practical balance point. They provide enough revisit opportunities to support time-sensitive AI inference without exhausting onboard power or requiring aggressive downlink scheduling. In essence, the composite efficiency score offers more than just a number—it helps identify orbits that align with the practical realities of edge-AI-enabled satellite missions.

Summary of the results Simulation results suggest that while low-inclination orbits maximize visibility and SSO offers a strong energy margin, mid-inclination NSSO especially at 70° delivers the most effective balance for an energy-aware, AI-driven EO mission. These insights form the basis for the broader trade-off analysis in the next chapter.

Chapter 5
DISCUSSION AND CONCLUSION

This chapter analyzes and interprets the results presented in Chapter 4, focusing on the trade-offs between SSO and NSSOs in the context of an autonomous airplane detection mission. It discusses the implications of the simulation outcomes, identifies key conclusions, acknowledges study limitations, and outlines future directions for research.

5.1 *Analysis of Trade-offs*

The simulation results reveal a clear spectrum of mission strategies, where the optimal orbit is not universal but is instead dictated by a finely balanced trade-off between temporal coverage, data volume, and energy sustainability. Each orbital class represents a distinct operational philosophy.

The **SSO** embodies a conservative, low-risk strategy. Its chief advantage is consistency; by providing stable illumination [1, 12, 13], it simplifies the computer vision task for the onboard AI, minimizing ambiguities from varying shadows or glare that could otherwise degrade detection performance [11, 14]. However, this study confirms that this reliability comes at the cost of profound operational inflexibility. For a time-sensitive surveillance mission aimed at detecting unscheduled events, the SSO's rigid revisit schedule—offering only 10 daytime passes in 7 days—is a critical limitation. It is an orbit well-suited for systematic monitoring, not responsive detection.

The **NSSOs** represent a more agile, high-opportunity approach. The **45° NSSO**, which prioritized raw visibility, serves as a high-reward but high-risk option. It maximizes the probability of capturing transient events by providing the most frequent "looks" at the target. However, this aggressive data acquisition strategy drives power consumption to the system's operational ceiling. Such a narrow energy margin makes the mission vulnerable to periods of lower-than-expected solar power generation or unexpected subsystem power demands, jeopardizing long-term sustainability.

In this context, the **70° NSSO** emerged as the most operationally robust solution. Its efficiency likely stems from its orbital geometry relative to the target's mid-latitude location. Unlike the 45°

orbit, which is optimized for lower latitudes, or the near-polar SSO, the 70° inclination provides a high frequency of direct overflights of Incheon with favorable viewing angles. It strikes an optimal balance, providing significantly more detection opportunities than the SSO while maintaining a much healthier energy margin than the 45° NSSO. This makes it ideal for sustained, autonomous missions that require both frequent data points and operational resilience.

These findings shows the transformative role of **onboard edge computing**. Traditionally, the primary constraint for a high-revisit mission was the satellite's downlink capacity [4, 3]. Edge AI fundamentally shifts this paradigm, making the key constraints the onboard capacity for power generation and sustainable data processing [11, 21]. The 70° NSSO is viable precisely because edge computing decouples the high frequency of image acquisition from the historically high cost of data transmission [4]. This allows mission design to move beyond the rigidity of SSOs and fully leverage orbital dynamics to meet tactical goals, making the choice of orbit an integral component of the intelligent system itself.

5.2 *Conclusions*

From the simulation-based evaluation, three key conclusions emerge:

1. **Mid-inclination NSSOs, particularly at 70°, offer superior mission efficiency compared to SSO.** For AI-driven EO at mid-latitudes, these orbits deliver more usable data per unit of energy consumed, supporting frequent revisits without overwhelming power budgets.

2. **Optimal orbital design is inherently mission-dependent.** SSO suits missions with low data volume needs and strict lighting requirements. In contrast, low-inclination NSSOs are advantageous when maximizing coverage is critical, provided sufficient onboard energy is available. Balanced orbits like the 70° NSSO offer a pragmatic compromise.

3. **Onboard edge AI is essential for exploiting the full potential of high-opportunity orbits.** It minimizes the cost of frequent acquisitions and enables responsive, autonomous operations under energy constraints.

Ultimately, this thesis demonstrates that the paradigm for designing EO missions is evolving. For satellites enabled with edge AI, mission success hinges on an integrated design philosophy where

orbital mechanics and onboard intelligence are considered in unison. A well-matched orbital profile is not merely a mission parameter—it is a critical component of the autonomous system itself. Taken together, these insights suggest that future EO missions—especially those relying on real-time AI inference—should consider not just smarter sensors, but smarter orbits.

5.3 *Potential Applications*

This research bridges three traditionally independent areas in satellite mission design—orbital configuration, onboard AI inference, and energy-aware operation—into a unified evaluation framework. By quantifying how different LEO profiles affect both visibility and energy constraints, this work enables more mission-appropriate design decisions that account for operational trade-offs. Unlike conventional approaches that rely solely on fixed SSOs and ground-based inference, this framework demonstrates how mission performance can be improved through flexible orbit selection and onboard autonomy.

1. Autonomous Satellite Tasking for Dynamic Surveillance Zones. This framework can be used to design LEO missions that autonomously reconfigure surveillance tasks based on evolving targets. For example, a mid-inclination NSSOs enable varied illumination geometry and more frequent coverage over mid-latitude regions. By optimizing orbits for better visibility and enabling real-time AI inference onboard, satellites can prioritize specific zones dynamically—without waiting for downlink or manual tasking from ground control. This is particularly useful for monitoring sensitive regions or shifting maritime zones where revisit frequency and autonomous decision-making are critical.

2. Rapid-Response Disaster Monitoring with Energy-Constrained Microsatellites. In post-disaster environments, ground communication infrastructure is often limited, and delays in response can be critical. By leveraging onboard inference and mission-specific orbit design, a satellite can autonomously detect damage signatures (e.g., destroyed infrastructure, wildfire fronts) in daylight conditions, even when energy resources are constrained. This research shows how certain mid-inclination NSSOs can outperform SSOs in capturing more frequent and energy-efficient observations during the daylight cycle—making them ideal for deploying low-cost microsatellites in emergency-response constellations.

5.4 *Limitations of the Study*

While this study provides a foundational methodology, the following limitations should be acknowledged as they offer context for the results and guide future work:

- **Hardware and Energy Modeling:** The analysis relied on benchmarked performance and power consumption data for the NVIDIA Jetson Xavier NX from technical specifications and prior studies. The simulation could not incorporate the real-time, dynamic power draw of the physical hardware, which may vary with computational load and thermal conditions.

- **Imaging and AI Model Assumptions:** A significant simplification was made by assuming ideal imaging conditions for the YOLOv5n model. The study did not account for real-world environmental factors such as clouds, rain, fog, or variable shadows, which would degrade image quality and negatively impact the AI's detection accuracy and processing time.

- **Mission and Simulation Scope:** The analysis was constrained to a single satellite and a 7-day simulation period. This scope precludes an analysis of constellation-level dynamics and does not account for long-term orbital perturbations like atmospheric drag.

- **Visibility and Viewing Geometry Criteria:** The study used a relatively relaxed minimum elevation angle of 20° to define a valid pass. A stricter constraint, such as nadir-only or near-nadir imaging, would yield higher-quality imagery but would drastically change the visibility and efficiency results.

- **Optical-Only Sensor Assumption:** This research exclusively modeled an optical payload, thereby constraining all viable imaging opportunities to daytime passes. This limitation neglects the potential for 24-hour surveillance, which is achievable with other technologies such as Infrared (IR) or Synthetic Aperture Radar (SAR) sensors that can operate at night and in adverse weather.

- **Simplified Orbit Propagation:** The orbital analysis used simplified assumptions, including circular orbits and a fixed argument of perigee (AOP = 0°). These constraints limited the scope

of orbital variation and excluded more complex orbital behaviors, such as eccentricity effects and non-trivial apsidal rotation, which may impact both visibility and energy dynamics in real missions.

5.5 *Future Research*

Building on the findings and limitations of this work, several avenues for future research could provide a more comprehensive understanding of this problem space:

- **Constellation Analysis:** Future work should analyze the performance of multi-satellite constellations in various SSO and NSSO configurations to evaluate system-level trade-offs in coverage and revisit time.

- **Advanced Energy and Hardware-in-the-Loop Modeling:** The energy model could be refined by integrating battery cycle modeling or by using a hardware-in-the-loop simulation to capture empirical power and thermal data from a physical Jetson Xavier NX.

- **Robust AI Performance under Variable Conditions:** Future research could model the impact of varying illumination and atmospheric conditions on AI detection accuracy, leading to a dynamic "image utility" metric that would refine the efficiency score.

- **Long-Term Orbital Simulations:** Extending the simulation period to months or years would be necessary to accurately model orbital decay and assess the impact of long-term perturbations on mission sustainability.

- **Analysis with Stricter Viewing Geometries:** The study should be repeated with more restrictive viewing constraints (e.g., near-nadir pointing) to assess the trade-off between higher-quality data and reduced access opportunities.

- **Incorporating All-Weather and Night-Vision Sensors:** The analysis could be expanded to include SAR or high-resolution thermal IR payloads. This would enable a 24-hour, all-weather mission profile, fundamentally altering the definition of a "useful" pass and introducing new,

complex trade-offs between the significantly different power requirements, data rates, and processing demands of these advanced sensors.

- **Expanded Orbital Parameter Space:** Future studies should extend the simulation framework to incorporate more diverse and realistic orbital configurations. This includes exploring elliptical orbits, varying argument of perigee, and incorporating precession effects beyond J2, allowing for a richer comparison of operational trade-offs across different mission profiles.

BIBLIOGRAPHY

[1] H. D. Curtis, *Orbital Mechanics for Engineering Students*. Oxford, UK: Butterworth-Heinemann / Elsevier, 4th ed., 2020.

[2] T. M. Lillesand, R. W. Kiefer, and J. W. Chipman, *Remote Sensing and Image Interpretation*. Wiley, 7th ed., 2015.

[3] A. V. Etten, J. Shermeyer, R. Nair, and J. Davis, "Aircraft Detection at Planetary Scale," March 2025. [Online]. Available: https://www.planet.com/pulse/aircraft-detection-at-planetary-scale/. Accessed: 2025-04-30.

[4] Y. Wang, J. Yang, X. Guo, and Z. Qu, "Satellite Edge Computing for the Internet of Things in Aerospace," *Sensors*, vol. 19, no. 20, p. 4375, 2019. https://doi.org/10.3390/s19204375.

[5] R. Bayer, J. Priest, and P. Tözün, "Reaching the Edge of the Edge: Image Analysis in Space," in *Proceedings of the Eighth Workshop on Data Management for End-to-End Machine Learning*, (New York, NY, USA), pp. 29–38, Association for Computing Machinery, 2024. https://doi.org/10.1145/3650203.3663330.

[6] Y. Shen, D. Liu, J. Chen, Z. Wang, Z. Wang, and Q. Zhang, "On-Board Multi-Class Geospatial Object Detection Based on Convolutional Neural Network for High Resolution Remote Sensing Images," *Remote Sensing*, vol. 15, no. 16, p. 3963, 2023. https://doi.org/10.3390/rs15163963.

[7] S. El Ghazouali, A. Gucciardi, F. Venturini, N. Venturi, M. Rueegsegger, and U. Michelucci, "FlightScope: An Experimental Comparative Review of Aircraft Detection Algorithms in Satellite Imagery," *Remote Sensing*, vol. 16, no. 24, p. 4715, 2024. https://doi.org/10.3390/rs16244715.

[8] J. Manning, D. Langerman, B. Ramesh, E. Gretok, C. Wilson, A. George, J. MacKinnon, and G. Crum, "Machine-Learning Space Applications on SmallSat Platforms with TensorFlow," in *Proceedings of the 32nd Annual AIAA/USU Conference on Small Satellites*, (Logan, UT, USA), 2018. Paper SSC18-WKVII-03.

[9] P. Zhao, X. Ye, and Z. Du, "Object Detection in Multispectral Remote Sensing Images Based on Cross-Modal Cross-Attention," *Sensors*, vol. 24, no. 13, p. 4098, 2024. https://doi.org/10.3390/s24134098.

[10] E. Kulu, "CubeSats & Nanosatellites—2024 Statistics, Forecast and Reliability," in *Proceedings of the International Astronautical Congress, IAC*, (Milan, Italy), October 2024.

[11] A. Duggan, B. Andrade, and H. Afli, "Advancing Earth Observation: A Survey on AI-Powered Image Processing in Satellites." arXiv preprint arXiv:2501.12030. Available: https://arxiv.org/abs/2501.12030, 2025.

[12] European Space Agency (ESA), "Types of orbits." [Online]. Available: https://www.esa.int/Enabling_Support/Space_Transportation/Types_of_orbits. Accessed: 2025-08-14.

[13] National Aeronautics and Space Administration (NASA) Earth Observatory, "Catalog of Earth Satellite Orbits." [Online]. Available: https://earthobservatory.nasa.gov/features/OrbitsCatalog. Accessed: 2025-08-14.

[14] A. Tahir, H. S. Munawar, J. Akram, M. Adil, S. Ali, A. Z. Kouzani, and M. A. P. Mahmud, "Automatic Target Detection from Satellite Imagery Using Machine Learning," *Sensors*, vol. 22, no. 3, p. 1147, 2022. https://doi.org/10.3390/s22031147.

[15] N. Thapa, A. K. Krishnakumar, N. B. Sharma, A. Sarkar, and S. S. Sarkar, "Simulation study on inclined orbit constellation of high-resolution electrooptical sensors for enhanced imaging efficiency in region of interest," *Journal of Applied Remote Sensing*, vol. 16, no. 3, p. 037503, 2022. https://doi.org/10.1117/1.JRS.16.037503.

[16] S. Treblow and C. N. McGrath, "Responsive Maneuver Planning for Sun-Synchronous Repeating Ground Track Orbits," *Journal of Spacecraft and Rockets*, vol. 62, no. 1, pp. 150–158, 2025. https://doi.org/10.2514/1.A35859.

[17] H. Lin, A. Parsi, D. Mullins, J. Horgan, E. Ward, C. Eising, P. Denny, B. Deegan, M. Glavin, and E. Jones, "A Study on Data Selection for Object Detection in Various Lighting Conditions for Autonomous Vehicles," *Journal of Imaging*, vol. 10, no. 7, p. 153, 2024. https://doi.org/10.3390/jimaging10070153.

[18] B. Potin, "Scheduling Earth Observing Satellites with Evolutionary Algorithms," tech. rep., NASA, 2003. [Online]. Available: https://ntrs.nasa.gov/api/citations/20030062898/downloads/20030062898.pdf. Accessed: 2025-08-14.

[19] N. Erdenebaatar, J. Kim, and T. Kim, "Analysis of Geometric and Spatial Image Quality of KOMPSAT-3A Imagery in Comparison with KOMPSAT-3 Imagery," *Korean Journal of Remote Sensing*, vol. 33, no. 1, pp. 1–13, 2017. https://doi.org/10.7780/kjrs.2017.33.1.1.

[20] C. Elachi and J. Van Zyl, *Introduction to the Physics and Techniques of Remote Sensing*. Hoboken: Wiley, 3rd ed., 2021.

[21] M. J. Veyette, K. Aylor, D. Stafford, M. Herrera, S. Jumani, C. Lineberry, C. Macklen, E. Maxwell, R. Stiles, and M. Jenkins, "AI/ML for Mission Processing Onboard Satellites," in *AIAA SciTech 2022 Forum*, American Institute of Aeronautics and Astronautics, 2022. Published online: December 29, 2021; Presented: January 3, 2022. https://doi.org/10.2514/6.2022-1472.

[22] M. O. Del Castillo, J. Morgan, J. Mcrobbie, C. Therakam, Z. Joukhadar, R. Mearns, S. Barraclough, R. Sinnott, A. Woods, C. Bayliss, K. Ehinger, B. Rubinstein, J. Bailey, A. Chapman, and M. Trenti, "Mitigating Challenges of the Space Environment for Onboard Artificial Intelligence: Design Overview of the Imaging Payload on SpIRIT," in *Proceedings of the IEEE/CVF Conference on Computer Vision and Pattern Recognition (CVPR) Workshops*, pp. 6789–6798, June 2024. https://doi.org/10.48550/arXiv.2404.08399.

[23] G. Furano, G. Meoni, A. Dunne, D. Moloney, V. Ferlet-Cavrois, A. Tavoularis, J. Byrne, L. Buckley, M. Psarakis, K.-O. Voss, and L. Fanucci, "Towards the Use of Artificial Intelligence on the Edge in Space Systems: Challenges and Opportunities," *IEEE Aerospace and Electronic Systems Magazine*, vol. 35, no. 12, pp. 44–56, 2020. https://doi.org/10.1109/MAES.2020.3008468.

[24] NVIDIA Corporation, "NVIDIA Jetson Nano Developer Kits," 2025. [Online]. Available: https://www.nvidia.com/en-us/autonomous-machines/embedded-systems/jetson-nano/product-development/. Accessed: 2025-08-14.

[25] NVIDIA Corporation, "NVIDIA Jetson AGX Xavier Series," 2025. [Online]. Available: https://www.nvidia.com/en-us/autonomous-machines/embedded-systems/jetson-xavier-series/. Accessed: 2025-08-14.

[26] G. Jocher, "YOLOv5 by Ultralytics," 2020. Version 7.0. doi:10.5281/zenodo.3908559. [Online]. Available: https://github.com/ultralytics/yolov5. Accessed: 2025-08-14.

[27] KOREA AEROSPACE RESEARCH INSTITUTE (KARI) and SI IMAGING SERVICES Co., LTD., *KOMPSAT-3 PRODUCTS SPECIFICATION Image Data Manual*, July 2015. Version 1.2.

[28] European Space Agency, "KOMPSAT-3 (Korea Multi-Purpose Satellite-3) / Arirang-3." eoPortal. [Online]. Available: https://www.eoportal.org/satellite-missions/kompsat-3. Accessed: 2025-08-14.

[29] C. Benedek and D. Kiss, "HRPlanesv2 - High Resolution Satellite Imagery for Aircraft Detection," 2022. Zenodo. doi:10.5281/zenodo.7331974. [Online]. Available: https://zenodo.org/record/7331974. Accessed: 2025-08-14.

[30] Z.-Q. Zhao, P. Zheng, S.-T. Xu, and X. Wu, "Object Detection With Deep Learning: A Review," *IEEE Transactions on Neural Networks and Learning Systems*, vol. 30, no. 11, pp. 3212–3232, 2019. https://doi.org/10.1109/TNNLS.2018.2876865.

[31] M. Pritt and G. Chern, "Satellite Image Classification with Deep Learning," in *2017 IEEE Applied Imagery Pattern Recognition Workshop (AIPR)*, pp. 1–7, 2017. https://doi.org/10.1109/AIPR.2017.8457969.

[32] C.-Y. Wang and H.-Y. M. Liao, "YOLOv1 to YOLOv10: The Fastest and Most Accurate Real-time Object Detection Systems," *APSIPA Transactions on Signal and Information Processing*, vol. 13, p. e29, 2024. https://doi.org/10.1561/116.20240058.

[33] J. Jeong, J. Kim, T. Kim, and S. Rhee, "Evaluation of the performance of KOMPSAT-3 stereo images in terms of positioning and the generation of digital surface models," *Remote Sensing Letters*, vol. 7, no. 10, pp. 955–964, 2016. https://doi.org/10.1080/2150704X.2016.1201223.

[34] S. W. Paek, S. Kim, L. Kronig, and O. de Weck, "Sun-synchronous repeat ground tracks and other useful orbits for future space missions," *The Aeronautical Journal*, vol. 124, no. 1276, pp. 917–939, 2020. https://doi.org/10.1017/aer.2020.21.

[35] I. Rodriguez-Ferrandez, M. Tali, L. Kosmidis, M. Rovituso, and D. Steenari, "Sources of Single Event Effects in the NVIDIA Xavier SoC Family under Proton Irradiation," in *2022 IEEE 28th International Symposium on On-Line Testing and Robust System Design (IOLTS)*, pp. 1–7, 2022. https://doi.org/10.1109/IOLTS56730.2022.9897236.

[36] J. Lee, E. Kim, and K. G. Shin, "Design and Management of Satellite Power Systems," in *2013 IEEE 34th Real-Time Systems Symposium*, pp. 97–106, 2013. https://doi.org/10.1109/RTSS.2013.18.

[37] I. Mavromatis, K. Katsaros, and A. Khan, "Computing Within Limits: An Empirical Study of Energy Consumption in ML Training and Inference," 2024. arXiv preprint arXiv:2406.14328. Available: https://arxiv.org/abs/2406.14328.

[38] Office of Civil Aviation, Republic of Korea, "Republic of korea aeronautical information publication (aip)," AIP Amendment NR 6/25, Ministry of Land, Infrastructure and Transport, Republic of Korea, 11, Doum 6-ro, Sejong-si, 30103, Republic of Korea, May 2025. Information regarding Incheon International Airport (ICN) airspace and coordinates (e.g., ARP 372745N 1262621E). Retrieved from https://aim.koca.go.kr.

[39] F. L. Markley and J. L. Crassidis, *Fundamentals of Spacecraft Attitude Determination and Control*. New York, NY: Springer, 2014.

[40] B. Huang, D. Reichman, L. M. Collins, K. Bradbury, and J. M. Malof, "Tiling and Stitching Segmentation Output for Remote Sensing: Basic Challenges and Recommendations," 2019. arXiv preprint arXiv:1805.12219. Available: https://arxiv.org/abs/1805.12219.

[41] H. Tang, X. Liang, L. Liu, and Z. Zhang, "Special Vehicle Target Detection Based on Improved Yolov5 + Jetson NX," in *2022 5th International Conference on Information Communication and Signal Processing (ICICSP)*, pp. 239–243, 2022. https://doi.org/10.1109/ICICSP55539.2022.10050613.

[42] A. Bessios and W. Hopkins, "High Data Rate Downlink Telemetry in Space Communications with Compact Spectral Containment," in *ICC 2021 - IEEE International Conference on Communications*, pp. 1–6, 2021. https://doi.org/10.1109/ICC42927.2021.9500937.

[43] L3Harris Technologies, "L3Harris SpaceView-80 Optical Payload," 2021. [Online]. Available: https://www.l3harris.com/sites/default/files/2021-06/l3harris-spaceview-brochure-sas.pdf. Accessed: 2025-08-14.

[44] S. Kang, Y. Gao, Y. Song, R. Zhou, and J. Pang, "Parameter probabilistic prediction for satellite power system based on unsupervised multi-dimensional sequence segmentation," *Aerospace Science and Technology*, vol. 146, p. 108933, 2024. https://doi.org/10.1016/j.ast.2024.108933.

[45] R. Dai, M. Wang, and Z. Ye, "Near-Real-Time Long-Strip Geometric Processing without GCPs for Agile Push-Frame Imaging of LuoJia3-01 Satellite," *Remote Sensing*, vol. 16, no. 17, p. 3281, 2024. https://doi.org/10.3390/rs16173281.

[46] STT-SystemTechnik GmbH, "SSTRX-1000 S-Band Satellite Transceiver," 2021. Technical Datasheet. [Online]. Available: https://www.stt-systemtechnik.de/en/products/space/tmtc-/-ttc/sstrx-1000/. Accessed: 2025-08-14.

Appendix A

CODE AND RESOURCE ACCESS

The simulation code, models, and data used in this thesis are available on GitHub. This includes orbit propagation scripts, energy consumption models, visibility analysis code, and visualization tools.

- GitHub Repository:

  github.com/umji4500/Master-Thesis

If access is restricted, please contact the author for collaboration or viewing rights.